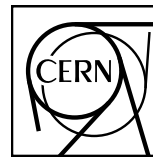


1



ALICE Scientific Note 2012-xxx
June 30, 2016

2

3

J/ψ production in Pb-Pb collisions at $\sqrt{s_{NN}} = 5.02$ TeV

4

R. Arnaldi, B. Audurier, J. Castillo, V. Feuillard, B. Paul, P. Pillot, E. Scomparin, M. Tarhini

5

alice-pag-dq-Jpsi2mumu@cern.ch

1 Introduction

In this note the analysis of the J/ψ production in Pb-Pb collisions at $\sqrt{s_{NN}} = 5.02$ TeV is presented. J/ψ are studied, in the rapidity range $2.5 < y < 4$, through their decay into a muon pair, with the muons being reconstructed in the Muon Spectrometer of the ALICE experiment. The J/ψ production is studied via the nuclear modification factor R_{AA} as a function of the collision centrality and as a function of the J/ψ transverse momentum. Results are compared with previous ALICE measurement at $\sqrt{s_{NN}} = 2.76$ TeV [1] and with the available theoretical predictions.

2 Data and event selection

The results presented in this analysis note are based on the 2015 Run-2 Pb-Pb data taking at $\sqrt{s_{NN}} = 5.02$ TeV, which took place in November-December 2015. Further informations might be found in the following Twiki page:

<https://twiki.cern.ch/twiki/bin/viewauth/ALICE/JPsiPbPb2015Raa>

2.1 The ALICE detector

A presentation of the ALICE detectors used in the J/ψ nucleus-nucleus analysis can be found in [2] and further details on the muon reconstruction technique are discussed in [1].

2.2 Data sample

The analysed Pb-Pb period (LHC15o muon calo pass1) contains 137 runs which have been QA checked. The list of the runs, used in this analysis, can be found in:

<https://twiki.cern.ch/twiki/bin/viewauth/ALICE/MuonPbPbQA2015>

The AOD set used in this analysis is AOD175.

2.3 Event selection

The event selection is the standard one which has usually adopted for charmonium studies. Details can be found in [1].

In order to select a clean data sample, only events passing the physics selection cuts are kept. Furthermore, we select events where the unlike sign low- p_T ($p_{T\mu}^{trigger} \geq 1$ GeV/c on each muon) dimuon trigger is fired (CMUL trigger). On the opposite sign dimuons and on the single muon track level, the standard cuts, usually adopted in the J/ψ analysis, have been applied, namely:

- $2.5 < y_{J/\psi} < 4$, to cope with the spectrometer's acceptance
- $2.5 < \eta_\mu < 4$ on both muons belonging to the dimuon, to reject tracks at the edges of the acceptance
- $17.6 < R_{abs} < 89.5$, where R_{abs} is the radial transverse position of the muon tracks at the end of the absorber, to remove tracks crossing the thicker part of the absorber
- both muon tracks reconstructed in the tracking chambers should match a trigger track reconstructed in the trigger system, above the low $p_T^{trigger}$ threshold.
- p_T of the J/ψ in $0 < p_T < 12$ GeV/c

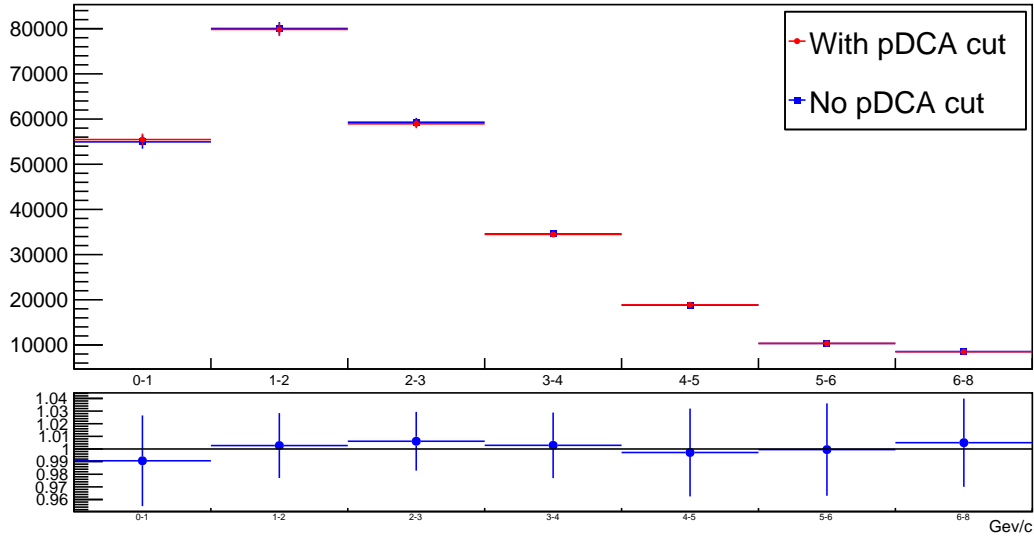


Fig. 1: Number of J/ψ extracted with and without the pDCA cut and the corresponding ratio.

40 The effect of the pDCA cut (tuned on the 2015 data) has also been investigated, but it turned out to be negligible in the J/ψ mass range as visible in Fig. 1. The number of measured J/ψ , in fact, vary at the per mille level, if the pDCA cut is applied and, therefore, the cut has not been applied in this analysis.

45 J/ψ candidates are obtained combining opposite sign muon pairs reconstructed within the geometrical acceptance of the spectrometer. The single muon tracks cuts previously described reduce the contribution of most of the hadrons escaping or produced in the front absorber, as well as the low p_T muons from pions and kaons decays, secondary muons produced in the front absorber and fake tracks.

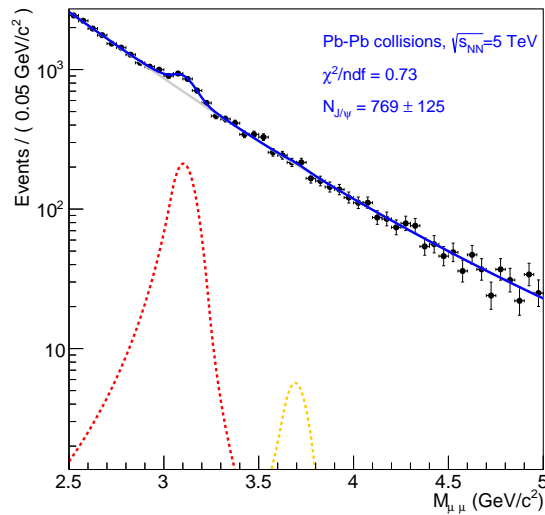


Fig. 2: Invariant mass spectrum in CMLL trigger, integrated over p_T and in centrality (0-90%). The number of J/ψ has been extracted with the fitting technique described in the next section.

Finally, the analysed data sample is based on the CMUL trigger. We have, nevertheless, checked if there are J/ψ events in the like-sign dimuon sample (CMLL), as it was the case during the 2011 data taking.

The CMLL triggers were not downscaled during the data taking. As it can be see in Fig. 2, the amount of J/ ψ in CMLL trigger, extracted with a fitting technique, as described in the next section, is negligible and it amounts to $\sim 0.3\%$. The issue of the small number of opposite sign dimuons misidentified by the trigger algorithm has also been extensively studied in the high statistics pp data sample at 13 TeV, as discussed in <https://aliceinfo.cern.ch/Notes/node/497>. The remaining bias is very small in pp and it is expected to be even more negligible in PbPb collisions, where both opposite and like sign triggers are more likely fired together given the increased multiplicity.

The J/ ψ production has been studied as a function of the centrality of the collisions. The centrality has been determined using the V0 detectors, having verified the flatness of the V0 distributions, in CINT7 trigger, versus time. The stability of the centrality determination can be observed in Fig. 3 for two classes of centrality.

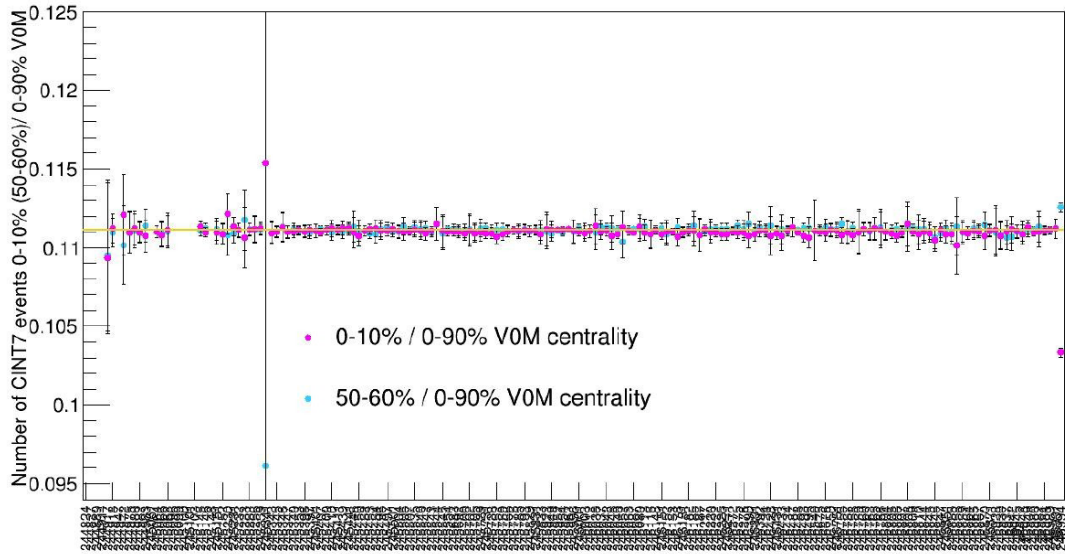


Fig. 3: Ratio of two centrality classes, i.e. 0–10% and 50–60%, with respect to the whole centrality range (0–90%) as a function of the run number (several runs later discarded are still included in this plot)

3 Signal Extraction

After applying the single muon and dimuon cuts mentioned in section 2 on the raw data from the 137 QA-accepted runs in `/alice/data/2015/LHC15o/* /muon_calor_pass1/AOD175/`, the signal extraction has been performed in two methods:

3.1 Direct Fit

With this method, the J/ψ yield is extracted through a fit of the dimuon invariant mass distribution. The fit function is the sum of two components that describe the signal shape and the background one.

For the signal shape, two functions have been used, the double extended Crystal-Ball (CB2) and the NA60 function.

For the background description, different functions have been tested. Because of the very high statistics and especially for the most central bins and the lowest p_T bins, only two functions seemed to work for all the bins in p_T , rapidity and centrality. The first one is a ratio of two polynomials of second and third orders (Pol(2)/Pol(3)), the second one is a quadratic variable width Gaussian (VWG). Others functions that are tested like the $Pol(4) \times Expo$ are not used since they gave a large fit goodness (χ^2/NDF). Having a high statistics data sample, the phenomenological background description we adopt is rather difficult, in particular over a broad mass range. Therefore, to avoid instabilities in the fitting approach, the fit is not performed in the invariant mass interval (e.g. [2,5] GeV/ c^2). Fits are performed in the mass ranges [2.2,4.5] and [2.4,4.7] GeV/ c^2 .

The analytic description of the used functions can be found in Appendix A. Examples of the fits are shown in Figure 4

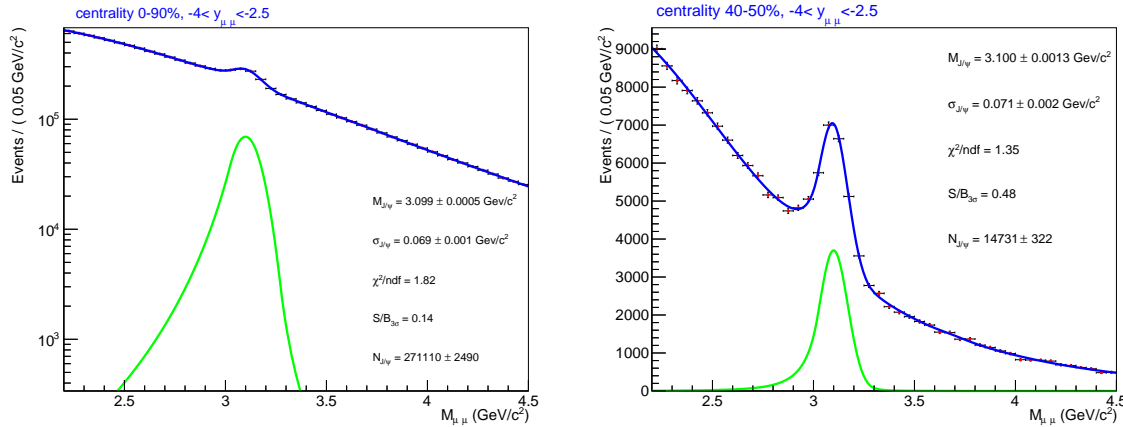


Fig. 4: Dimuon invariant mass distributions. In the left panel, the spectrum is integrated over centrality, in the right one it refers to the 40-50 % centrality range. The distributions are fitted with a sum of an extended Crystal-Ball function and Pol(2)/Pol(3) one

3.2 Fit After The Event-Mixing

The idea behind the event-mixing is to subtract the contribution from the so called combinatorial background before performing a fit to the dimuon invariant mass distribution. In Pb-Pb collisions the main source of background is combinatorial which makes the fit easier if one subtract it.

In this analysis, the event-mixing is based on 10% centrality pools. It has been also shown that using

z-vertex pools alongside with the centrality ones, has no effect on the results.

The event-mixing has been done in two different methods. For both methods, we mix each muon with muons in previous events (in the same pool and same run). In the first method, we stop mixing when we get 20 mixed dimuons for each muon. In the second method, we stop mixing at the 20th previous event. The results from the two methods were in very good agreement.

3.2.1 Normalization

To normalize the mixed events spectra to the raw ones, three methods have been tested:

$$- 1- F = \frac{\int_2^{2.5} N_{Raw}^{+-} dm + \int_4^5 N_{Raw}^{+-} dm}{\int_2^{2.5} N_{Mix}^{+-} dm + \int_4^5 N_{Mix}^{+-} dm}$$

$$- 2- F = \frac{\int_2^8 2R \sqrt{N_{Raw}^{++} N_{Raw}^{--}} dm}{\int_2^8 N_{Mix}^{+-} dm}$$

$$- 3- F = \frac{\int_2^8 2R \sqrt{N_{Raw}^{++} N_{Raw}^{--}} dm}{\int_2^8 2R \sqrt{N_{Mix}^{++} N_{Mix}^{--}} dm}$$

where F is the normalization factor, the N s are the unlike-sign and like-sign spectra of the raw and mixed events, and R is a detector-related factor given by $R = \frac{N_{Mix}^{+-}}{2\sqrt{N_{Mix}^{++} N_{Mix}^{--}}}$, where its value is ≈ 1 in our integration range as it is shown in the Figure 6.

In Table 5 values of F , together with the number of mixed events are shown, for each centrality class.

centrality	number of mixed dimuons	F2	F3	F1
0-10	3.35354e+07	0.19745	0.19745	0.19917
10-20	2.14611e+07	0.15261	0.15262	0.15390
20-30	1.79047e+07	0.11109	0.11108	0.11312
30-40	1.37298e+07	0.07505	0.07505	0.07751
40-50	1.22631e+07	0.047613	0.047614	0.04983
50-60	6.24988e+06	0.026971	0.026972	0.02998
60-70	1.8268e+06	0.01425	0.01424	0.01757
70-80	1.20305e+06	0.00654	0.00655	0.010139
80-90	204811	0.00302	0.00302	0.00766

Fig. 5: Values of F , together with the number of mixed events, for each centrality class used in this analysis

The weakness point of the first method is that we exclude by hand the J/ ψ peak which means also that it has smaller integration range. The second and the third methods gave similar results and in the following, the used results correspond to the second one.

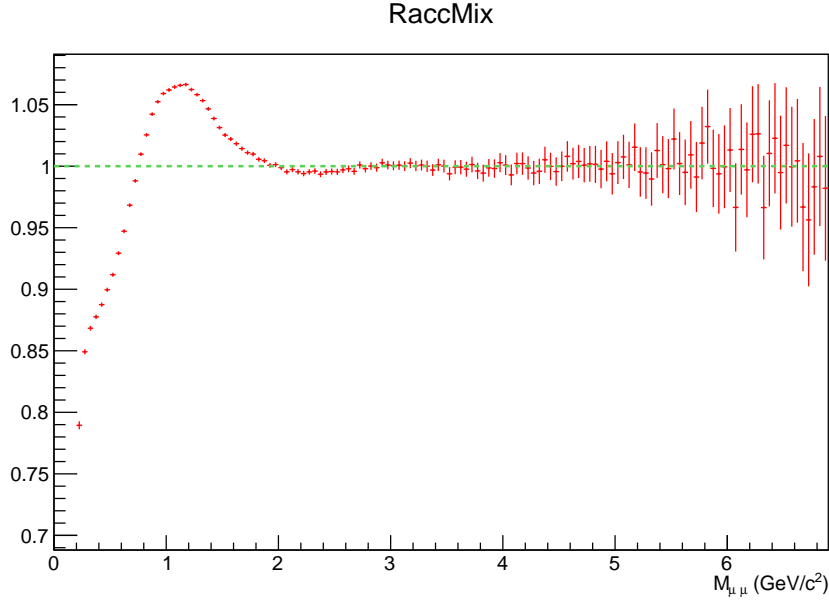


Fig. 6: The R factor obtained with mixed events for 0-10% centrality class

After the normalisation, the mixed spectra are subtracted from the raw ones, then the resulted distribution is fitted with a sum of two functions, a signal shape and another one to describe the residual background. For the signal shape, we use the same shapes as for the direct fit procedures (CB2 and NA60). For the residual background, a double exponential function is adopted since it worked well for the different invariant mass ranges. It can be pointed out that, given the small level of the background contribution, the choice of different background functions has a negligible impact. Examples of these fits on the subtracted spectra are shown in Figure 7.

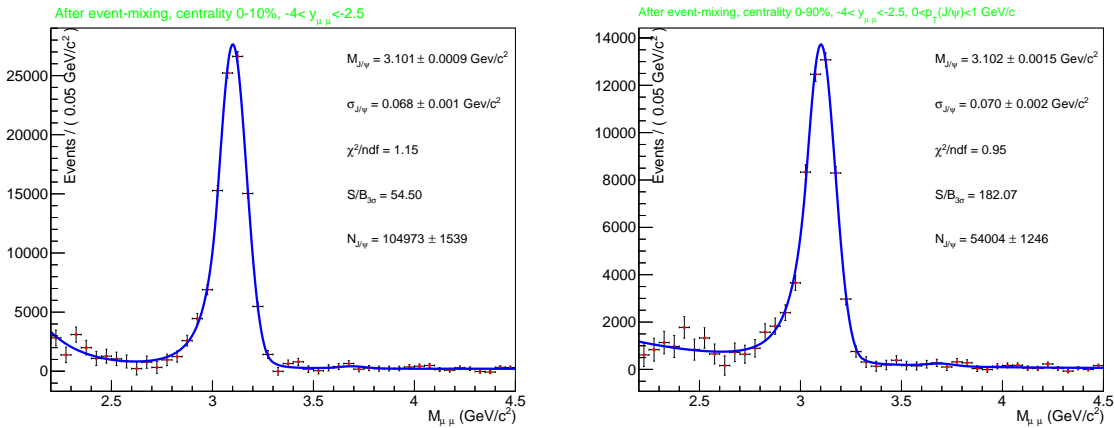


Fig. 7: Dimuon invariant mass distributions after the subtraction of the mixed spectra. In the left panel the spectrum corresponds to the 0-10% centrality, in the right one it is integrated in centrality for $0 < p_T < 1 \text{ GeV}/c^2$. The distributions are fitted with a sum of an extended Crystal-Ball function and a double-exponential one

3.3 Effect of the signal tails

The two functions used to describe the signal are the CB2 and NA60. Both functions have a Gaussian core in addition to left and right tails that account for detector physics processes like the energy-loss and

the Coulomb multiple scattering in the front absorber. Therefore changing the description of the detector in the simulation will result in different tails. Ideally one can let the parameters of those tails free when fitting the invariant mass spectra, but this is not feasible in Pb-Pb collisions due to the small signal over background ratio.

In this analysis, three sets of tails has been used for the signal extraction. The first set is obtained MC simulation with embedding (Section 5), in this simulation, the GEANT3 was used as a transport code. The second tails set was obtained from pure J/ ψ simulation using the GEANT4 as a transport code since it describes the geometry and the physics processes in a different way than GEANT3 so it is expected to give different tails. Finally the third set of tails is coming from pp at $\sqrt{s} = 13$ TeV J/ ψ analysis where fits are performed by letting the tail parameters free. Figure 8 shows three CB2 functions corresponding to the three tail sets.

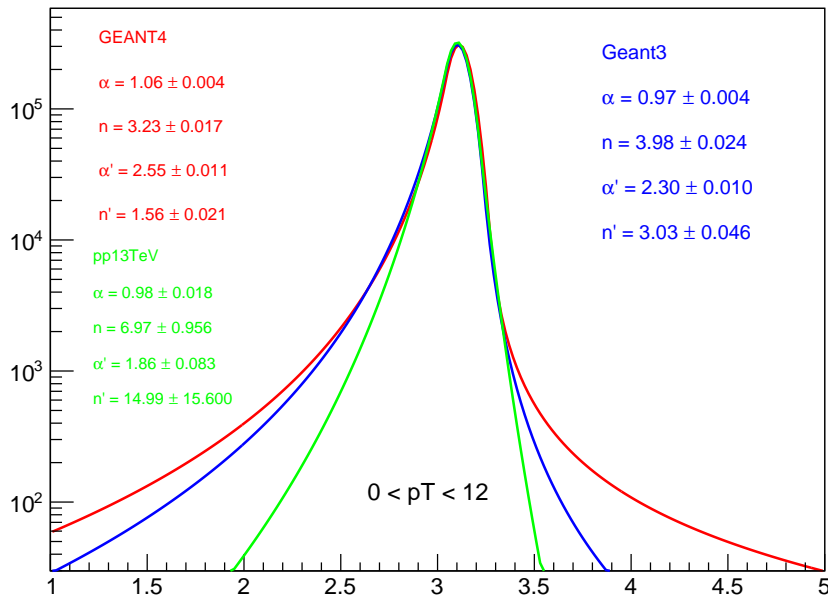


Fig. 8: In red and blue, CB2 functions obtained by fitting the dimuon invariant mass spectra of MC simulations using GEANT4 and GEANT3 as transport code. In green, a CB2 function with tails parameters obtained from pp at $\sqrt{s} = 13$ TeV

3.4 Systematic Uncertainty

It has been observed that the fit is affected by varying the fit range, therefore two fit ranges have been used, [2.2,4.5] and [2.4,4.7] GeV/ c^2 for the first method (direct fit). For the fit after even-mixing, the fit range [2,5] GeV/ c^2 has been also included. For the CB2 function, the three sets of tails mentioned above have been used, while for the NA60 only the two sets from the MC simulation have been used since the pp @ 13 TeV tails are not available for this function.

This resulted in 20 tests $\{(2 \text{ fit ranges}) \otimes (2 \text{ background functions}) \otimes (2 \text{ NA60 tail sets} + 3 \text{ CB2 tail sets})\}$ with the first method, and 15 tests $\{(3 \text{ fit ranges}) \otimes (2 \text{ NA60 tail sets} + 3 \text{ CB2 tail sets})\}$ with the second method. Each test gave a J/ ψ yield and the final yield is provided by the average of all the 35 yields. The systematic on the signal extraction is then given by the *RMS* of the yield distributions. To give a similar weight for data and MC tail sets, each test with pp at $\sqrt{s} = 13$ TeV tails has been weighted by 4 ($\{(2 \text{ MC sets}) \otimes (2 \text{ Signal functions})\}$) when calculating the average yield and *RMS*.

3.5 Results

3.5.1 Integrated Result

140 The Figure 9 shows the J/ψ yield distribution for the integrated invariant mass spectrum, and the final yield is $N_{J/\psi} = 277007 \pm 2434(stat) \pm 4806(sys)$. The statistical uncertainties between points are strongly correlated, since the fitted data are the same.

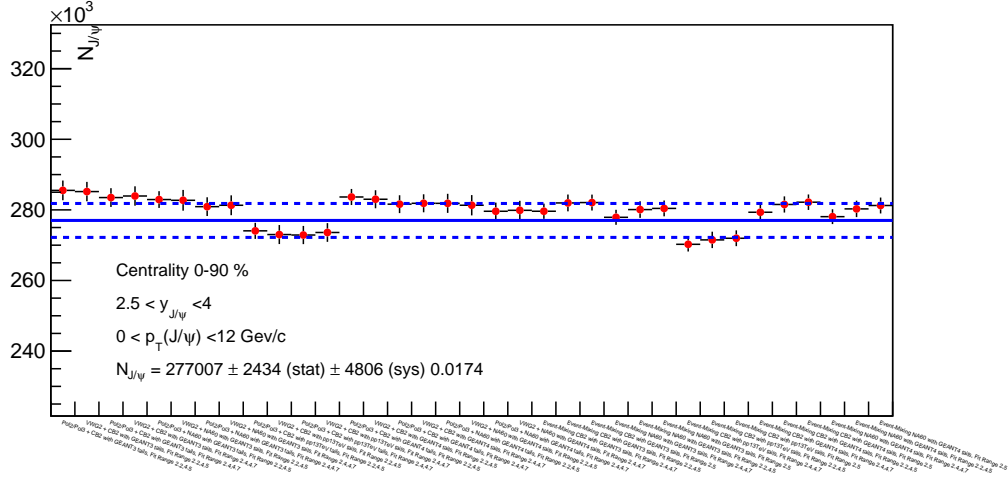


Fig. 9: Distribution of the J/ψ yield as a function of the signal extraction test for the integrated spectrum

3.5.2 In Centrality Bins

145 The signal extraction is performed in 9 centrality bins (10% each). The Table 1 shows the final yield in each centrality bin with both statistical and systematic uncertainty. It also shows these yields after applying a transverse momentum cut ($p_T > 0.3 \text{ GeV}/c$).

Centrality	$N_{J/\psi} \pm (stat) \pm (sys)$	Centrality	$N_{J/\psi} \pm (stat) \pm (sys)$
$-4 < y < -2.5, 0 < p_T < 12 \text{ GeV}/c$		$-4 < y < -2.5, 0.3 < p_T < 12 \text{ GeV}/c$	
0 , 10	$108070 \pm 1801 \pm 1996$	0 , 10	$105482 \pm 1763 \pm 2026$
10 , 20	$69808 \pm 1168 \pm 1161$	10 , 20	$68195 \pm 1201 \pm 1178$
20 , 30	$45007 \pm 822 \pm 728$	20 , 30	$43966 \pm 790 \pm 707$
30 , 40	$24876 \pm 491 \pm 630$	30 , 40	$24221 \pm 484 \pm 590$
40 , 50	$15010 \pm 321 \pm 281$	40 , 50	$14443 \pm 317 \pm 276$
50 , 60	$7895 \pm 190 \pm 147$	50 , 60	$7425 \pm 180 \pm 139$
60 , 70	$4112 \pm 105 \pm 71$	60 , 70	$3748 \pm 103 \pm 66$
70 , 80	$2042 \pm 66 \pm 34$	70 , 80	$1742 \pm 61 \pm 29$
80 , 90	$932 \pm 37 \pm 15$	80 , 90	$672 \pm 32 \pm 12$

Table 1: Average J/ψ yield with statistical and systematic uncertainties in each centrality bin.

With the high statistics that we have in 2015, we are able to do the signal extraction with finer bins in centrality. Table 2 shows shows the final yield in 24 centrality bins with their corresponding statistical and systematic uncertainties:

Centrality	$N_{J/\psi} \pm (stat) \pm (sys)$	Centrality	$N_{J/\psi} \pm (stat) \pm (sys)$
$-4 < y < -2.5, 0 < p_T < 12$ GeV/c		$-4 < y < -2.5, 0 < p_T < 12$ GeV/c	
0 , 2	$26506 \pm 935 \pm 636$	30 , 35	$14062 \pm 385 \pm 400$
2 , 4	$23564 \pm 851 \pm 545$	35 , 40	$10824 \pm 305 \pm 221$
4 , 6	$21871 \pm 802 \pm 372$	40 , 45	$8550 \pm 253 \pm 164$
6 , 8	$18565 \pm 674 \pm 402$	45 , 50	$6458 \pm 194 \pm 125$
8 , 10	$17866 \pm 622 \pm 415$	50 , 55	$4552 \pm 149 \pm 96$
10 , 12	$17143 \pm 631 \pm 391$	55 , 60	$3355 \pm 111 \pm 56$
12 , 15	$22037 \pm 697 \pm 387$	60 , 65	$2398 \pm 81 \pm 43$
15 , 18	$19337 \pm 631 \pm 412$	65 , 70	$1710 \pm 65 \pm 35$
18 , 21	$17621 \pm 538 \pm 431$	70 , 75	$1198 \pm 53 \pm 22$
21 , 24	$15074 \pm 510 \pm 300$	75 , 80	$848 \pm 41 \pm 16$
24 , 27	$13163 \pm 417 \pm 208$	80 , 85	$572 \pm 29 \pm 10$
27 , 30	$10922 \pm 354 \pm 214$	85 , 90	$351 \pm 22 \pm 7$

Table 2: Average J/ ψ yield with statistical and systematic uncertainties in smaller centrality bins.

150 3.5.3 In Rapidity Bins

Versus rapidity, the signal extraction is performed in six bins (of width $y=0.25$ each). The results for the final J/ ψ yield are presented in Table 3 .

Rapidity	$N_{jpsi} \pm (stat) \pm (sys)$
$centrality0 - 90\%, p_T > 0$ GeV/c	
-4 , -3.75	$11977 \pm 352 \pm 193$
-3.75 , -3.5	$41156 \pm 738 \pm 352$
-3.5 , -3.25	$64484 \pm 1029 \pm 383$
-3.25 , -3	$73975 \pm 1302 \pm 200$
-3 , -2.75	$59129 \pm 1133 \pm 709$
-2.75 , -2.5	$18485 \pm 659 \pm 449$

Table 3: Average J/ ψ yield with statistical and systematic uncertainties in each rapidity bin

3.5.4 In Transverse Momentum Bins

155 Results described in this analysis note are based on the pp reference based on the measured ALICE J/ ψ cross-sections results at $\sqrt{s} = 5.02$ TeV. This choice allows to extend the J/ ψ p_T coverage to $p_T = 12$ GeV/c. The Table 4 shows the final J/ ψ yield in each p_T bin, up to 12 GeV/c for the 0-90% and 0-20% collisions.

pT	$N_{j\psi} \pm (stat) \pm (sys)$
$-4 < y < -2.5, \text{centrality } 0-90\%$	
0, 1	$56178 \pm 1467 \pm 1148$
1, 2	$82293 \pm 1410 \pm 1378$
2, 3	$60165 \pm 988 \pm 1165$
3, 4	$34873 \pm 605 \pm 814$
4, 5	$19303 \pm 408 \pm 312$
5, 6	$10790 \pm 266 \pm 138$
6, 8	$8895 \pm 204 \pm 150$
6, 7	$5823 \pm 169 \pm 57$
7, 8	$2984 \pm 127 \pm 45$
8, 9	$1843 \pm 82 \pm 51$
9, 10	$1040 \pm 66 \pm 21$
10, 12	$937 \pm 62 \pm 19$

pT	$N_{j\psi} \pm (stat) \pm (sys)$
$-4 < y < -2.5, \text{centrality } 0-20\%$	
0, 1	$36836 \pm 1292 \pm 760$
1, 2	$55865 \pm 1256 \pm 1022$
2, 3	$39081 \pm 932 \pm 769$
3, 4	$21576 \pm 540 \pm 451$
4, 5	$11227 \pm 365 \pm 210$
5, 6	$6299 \pm 242 \pm 77$
6, 8	$4672 \pm 167 \pm 78$
6, 7	$3157 \pm 129 \pm 69$
7, 8	$1527 \pm 105 \pm 28$
8, 9	$998 \pm 71 \pm 28$
9, 10	$550 \pm 56 \pm 15$
10, 12	$542 \pm 45 \pm 17$

Table 4: Average J/ψ yield with statistical and systematic uncertainties in each p_T bin for 0-90% and 0-20% centrality

4 Normalization

In order to compute yields from the number of J/ ψ , one has to estimate the equivalent number of minimum bias events (N_{MB}^{eq}) from the number of triggered unlike-sign muon events (N_{MUL}) as :

$$N_{MB}^{eq} = \sum_{run=i} F_{norm}^i \times N_{MUL}^i \quad (1)$$

where F_{norm}^i is the normalisation factor computed run-by-run. Note that any other reaction channel for which the cross-section is known (instead of MB) can be used to normalise the J/ ψ yield measured in the MUL trigger data sample.

4.1 The F_{norm} calculation methods

One can think of several methods in order to compute the normalisation factor. But prior to the presentation of the different methods, we would like to introduce the pile-up factor PU since it appears in all the following sections. This factor is defined as :

$$PU^i = \frac{\mu^i}{1 - e^{-\mu^i}} \quad (2)$$

Being i the run number, this quantity is computed run-by-run. μ^i is defined as:

$$\mu^i = -\ln \left(1 - \frac{F_{purity}^{MB,i} \times LOb_{MB}^{rate,i}}{N_{colliding}^i \times f_{LHC}} \right) \quad (3)$$

where F_{purity}^{MB} is the purity factor associated to MB events , computed offline as the fraction of physics selected (PS) events for a given centrality range (CENT) divided by the total number of events :

$$F_{purity}^{MB,i} = \frac{N_{MB}(PS, CENT)}{N_{MB}(ALL, ALL)} \quad (4)$$

Note that the $LOb_{MB}^{rate,i}$ used to compute μ^i is directly taken from the OCDB scalers.

With those definitions in mind, we can now present the three methods used to extract the F_{norm} factor.

4.1.1 Offline Method 1 :

The first method is based on offline counters from offline data (namely ESDs or AODs). For each run i we compute F_{norm}^{offl} with the following formula :

$$F_{norm}^{offl,i} = PU^i \times \frac{MB^i}{MB \& 0MUL^i} \quad (5)$$

where

- MB is the number of physic selected (PS) minimum bias (MB) events.
- MB&0MUL is the subsample of MB event containing also a 0MUL input.
- PU is the pile-up correction factor associated to the MB trigger.

4.1.2 Offline Method 2 :

This method also is based on offline counters. To compute the normalisation factor between two triggers, one can take Eq. (5) and use an intermediate trigger with higher statistics (like the single muon trigger for example) :

$$F_{norm}^{off2,i} = PU^i \times \frac{MSL^i}{MSL \& 0MUL^i} \times \frac{MB^i}{MB \& 0MSL^i} \quad (6)$$

where

- MSL is the number of physic selected MSL events.
- MB&0MUL is the subsample of MSL events containing also a 0MUL L0 trigger.

Note that this method is particularly useful when the MUL trigger is low in statistics.

4.1.3 Online Scaler Method :

In the last method, one can use is to compute the F_{norm} relying on the L0b trigger scalers taken directly from the OCDB, which reads :

$$F_{norm}^{scal,i} = PU^i \times \frac{F_{purity}^{MB} L0b_{MB}^i}{F_{purity}^{MUL} L0b_{MUL}^i} \quad (7)$$

where F_{purity}^{MUL} is the purity factor associated to the unlike-sign muon trigger (MUL).

4.2 Results

For the period considered here, all the above methods have been computed tested directly from ESDs. The related triggers used for this analysis are :

- The CINT7-B-NOPF-MUFAST class, in 0–90%
- The C0V0M-B-NOPF-MUFAST class, a semi-central trigger class (0-60% centrality)
- The CMUL-B-NOPF-MUFAST class for $L0b_{MUL}$ and N_{MUL}
- The CMSL-B-NOPF-MUFAST class for the intermediate trigger MSL

The integrated luminosity of this period is $\sim 0.2 \text{ nb}^{-1}$. A more precise value of the integrated luminosity and its uncertainty is being evaluated.

4.2.1 Pile-up and purity factors

The pile-up correction factor for CINT7 is given in Figure 10. Note that the pile-up has also be evaluated without requiring the PS in the data sample. The purity correction factors for CINT7 and MUL are given in Figure 11. In the case of the C0V0M the PS for this class was not included in the partition. Hence the physics selection relies in the event being also triggered by another class, like CINT7, which is included in the PS (Figure 12). The purity factor is consistant with unity at the per-mille level except for one run. Thus, we assume it to be equal to 1 for the whole run period.

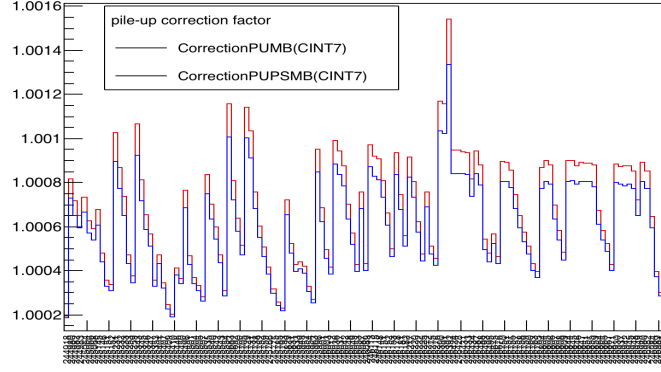


Fig. 10: Evolution of the pile-up correction factor for CINT7. The pile-up factor is given with (blue curve) and without physics selection (red curve)(PS).

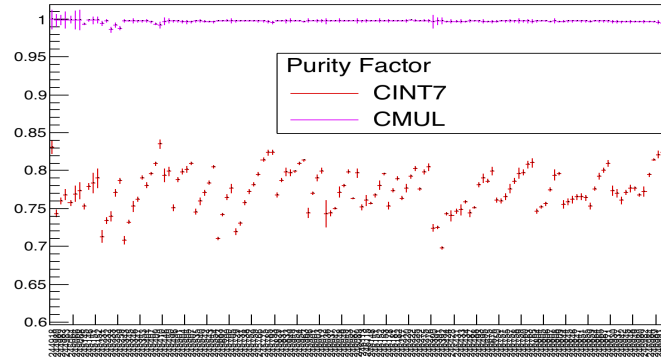


Fig. 11: Evolution of the purity factors for CINT7 and CMUL with the run period for CINT7.

4.2.2 Results

The F_{norm} for CINT7 is given in Figure 13. We can see a systematic shift (around 3%) for the scaler method compare to the two offline methods. This shift might be due to a contamination of the CINT7 L0 scalers by V0 after pulses, and it was the reason why we used the C0V0M semi-central trigger for the scaler method.

However, to compare CINT7 and C0V0M normalisation factors (i.e offline and online methods), we need to scale the C0V0M results to the same centrality range than the CINT7 (0-90%). Therefore, one should be sure that the cut at 60% centrality for the C0V0M is sharp. If we look at Figure 14 where the ratio of peripheral events over all the events is plotted run-by-run, we can see that it is not the case. There is a clear decreasing trend with increasing run number, typically due to the ageing of the V0, and one should apply this correction to the F_{norm}^{scal} for the C0V0M. If a is the ratio of peripheral events over all the events triggered by C0V0M, the corresponding scaler normalisation factor for centrality 0-90% ($F_{norm}^{scal}|_{0-90}$) becomes :

$$F_{norm}^{scal}|_{0-90} = F_{norm}^{scal} \times \frac{9(1-a)}{6} \quad (8)$$

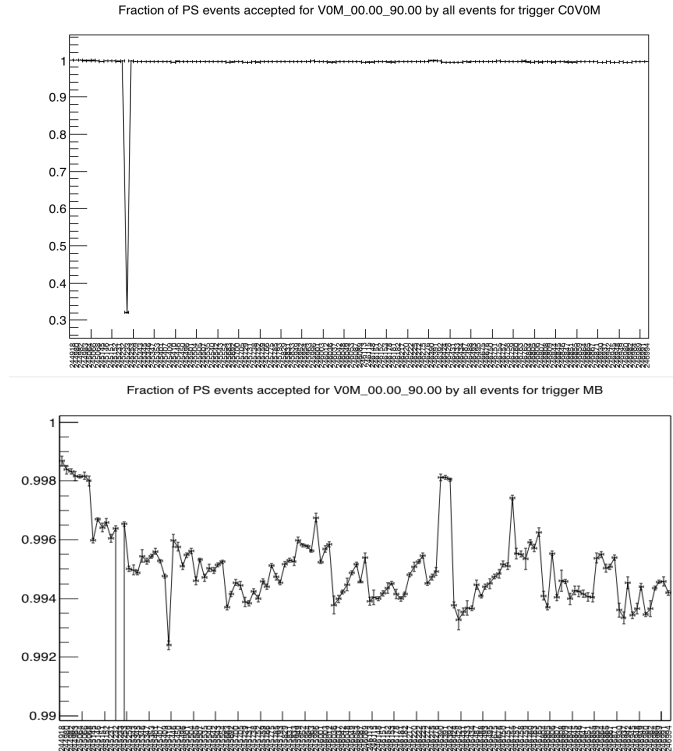


Fig. 12: Evolution of the purity factor for C0V0M. The bottom plot is a zoom of the top plot.

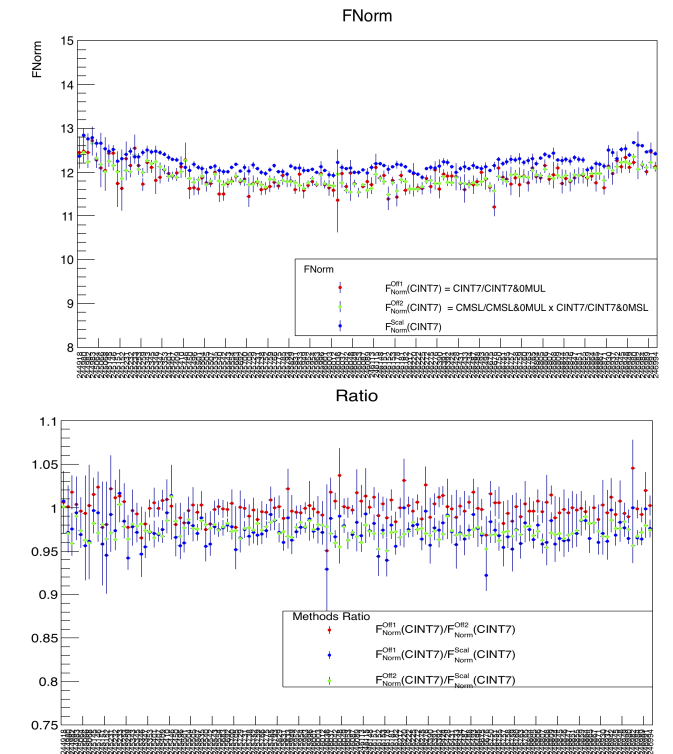


Fig. 13: Evolution of $F_{norm}(CINT7)$ for the three methods versus run numbers. One can note here a systematic shift of the scaler methods compared to the offline methods.

225 Final results are plotted in Figure 15. All the F_{norm} evaluations are consistent and in good agreement within statistical errors. Using Eq. 1, we can evaluate the number of equivalent minimum bias for all the

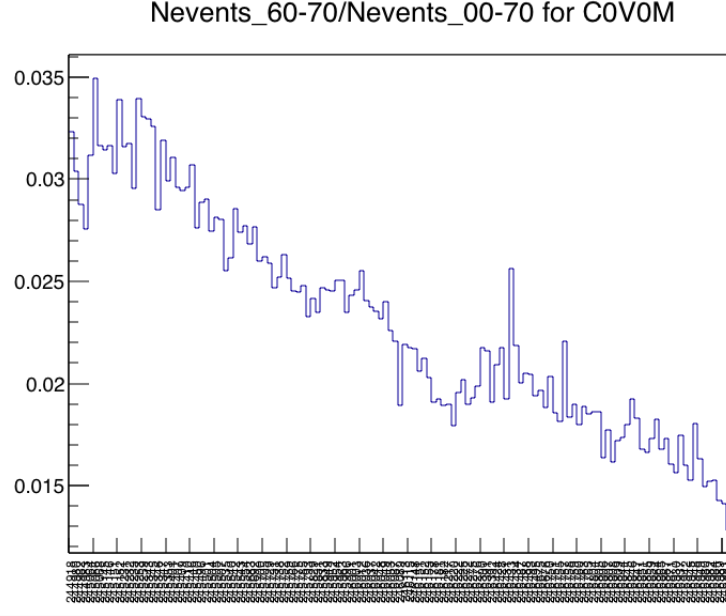


Fig. 14: Fraction of events between 60-70% centrality over events between 0-70% centrality, corresponding to a in Eq 8 . One can see a clear decreasing trend with increasing run numbers due to the V0 ageing.

three methods. Results are given in table 5. Again, all the methods are compatible within errors, and the weighted mean value of N_{MB}^{eq} is therefore dominated by the method with the smallest statistical error, namely $F_{norm}^{scal}(C0V0M)$, giving a weighted mean $F_{norm}^{mean} = 11.842 \pm 0.01\% (stat.) \pm 0.5\% (syst.)$. The systematic error has been put by hand at 0.5% to be conservative.

230

Method	F_{norm}	statistical error
$F_{norm}^{off1}(CINT7)$	11.845	0.10%
$F_{norm}^{off2}(CINT7)$	11.850	0.07%
$F_{norm}^{scal}(C0V0M)$	11.841	0.01%
weighted mean	11.841	0.01%

Table 5: Average value of Fnorm obtained with three different approaches and weighted mean.

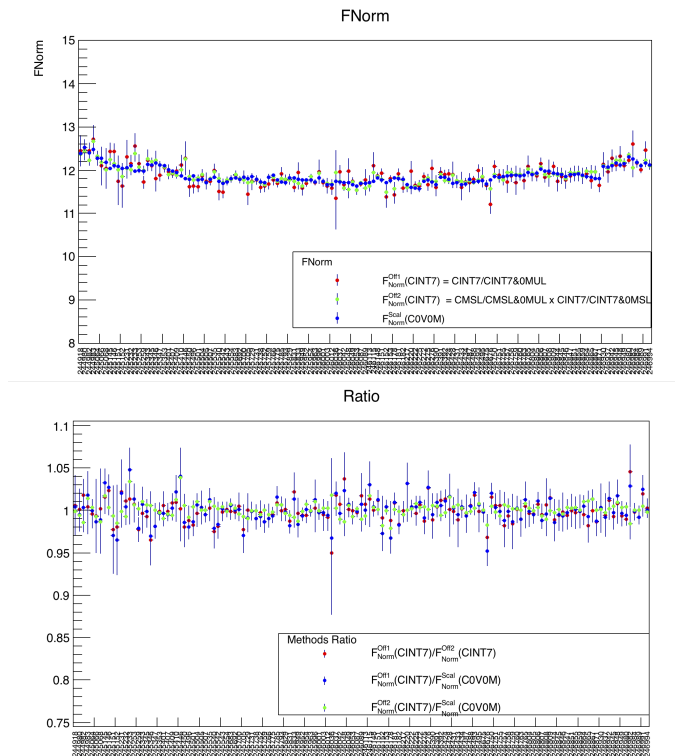


Fig. 15: Evolution of $F_{\text{norm}}(\text{CINT7})$ for the three methods versus run numbers. All the methods are in good agreement within statistical errors.

5 Acceptance

The J/ ψ acceptance \times efficiency (acc. \times eff.) have been obtained via a MC based on the embedding technique. More in details, one MC J/ ψ is embedded in each CINT7-B-NOPF-MUFAST event, for 80% of the chunks of each QA selected run. A total number of 1×10^6 J/ ψ has been reconstructed in the MC embedding. Since the embedding is done in CINT7 events, while in the analysis the CMUL7 events are selected, two weights are considered:

- a weight proportional to the number of CMUL7 triggers in each run, in order to take properly into account the run-by-run evolution of the acc. \times eff.
- a weight given by the raw number of reconstructed J/ ψ in each centrality bin, needed to correctly evaluate the centrality-integrated acc. \times eff.

The J/ ψ input shapes used in the embedding have been tuned directly on the centrality-integrated data (0-90%), corrected for the acceptance times efficiency, through an iterative procedure, similar to the one described in Fig. 23. The adopted input functions are, for the p_T distribution:

$$f(p_T) = p_0 * p_T / (1 + (p_T/p_1)^{p_2})^{p_3} \quad (9)$$

with $p_0=1.01 \cdot 10^6$, $p_1=3.50$, $p_2=1.93$, $p_3=3.96$ and for the rapidity distribution:

$$f(y) = p_0 * \exp(-0.5 * ((y - p_1)/p_2)^2) \quad (10)$$

with $p_0=1.10e6$, $p_1=0$, $p_2=2.13$

The J/ ψ production is assumed to be unpolarized. A further weight has been applied to the MC embedding acc. \times eff., to take into account the centrality dependence of the input shapes. In particular, given the high statistics collected in the 2015 Pb-Pb run, it has been possible to extract, directly from the acceptance corrected data, the J/ ψ p_T shapes (f_i) in several centrality bins and to use these distributions as weights for the embedding. In a given centrality bin i , the acc. \times eff. is evaluated as:

$$(Acc \times eff)_i = \frac{\sum_{p_T} (Acc \times eff)_{i,p_T}^{0-90\%} \times f_i(p_T)}{\sum_{p_T} f_i(p_T)} \quad (11)$$

where $(Acc \times eff)_{i,p_T}^{0-90\%}$ is the acceptance computed using as input the shapes tuned on data in 0-90%.

The J/ ψ p_T -differential shapes (in the range $0 < p_T < 12$ GeV/c), shown in Fig. 16, have been evaluated in seven centrality bins (0-10%, 10-20%, 20-30%, 30-40%, 40-50%, 50-60%, 60-90%). They have been corrected by the $(Acc \times eff)_{i,p_T}^{0-90\%}$ and then fitted, using the shape described by Eq. 9. It should be pointed out that for the most peripheral bin, a cut on the J/ ψ p_T ($p_T > 0.3$ GeV/c) has been applied, to reduce the contribution of photo-produced J/ ψ (it was shown that this cut removes $\sim 80\%$ of the photo-produced J/ ψ at $\sqrt{s_{NN}} = 5.02$ TeV). A comparison of the spectra obtained in the centrality bins and the one obtained integrating over centrality (0-90%) is shown in Fig. 17.

To verify the stability of the embedding correction based on $f_i(p_T)$, we have followed an iterative procedure. The number of J/ ψ , as a function of p_T and centrality, corrected, in the first step, by the $(Acc \times eff)_i^{0-90\%}$, are now corrected by the acc. \times eff. weighted to account for the centrality dependence of the J/ ψ transverse momentum distributions. The resulting J/ ψ yields are, then, used as a new weight to the Acc. \times efficiency computed with the MC embedding. Being the J/ ψ shapes very similar to those resulting from the first step, it has been verified that the effect of this second iteration is negligible: the acc. \times eff. resulting from the first and the second steps differ by less than 0.5%.

The resulting centrality dependence of the acc. \times eff. is shown in Fig. 18. The acc \times eff increases from central to peripheral collisions and the centrality dependence of the input shapes induces an increase of

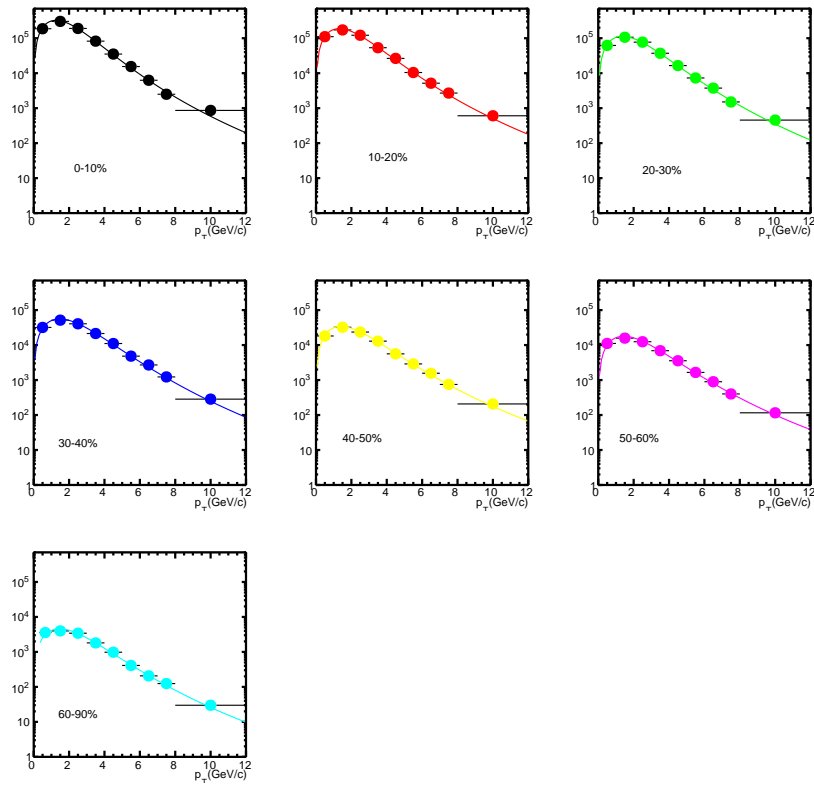


Fig. 16: J/ψ p_T -differential spectra, corrected by the acceptance \times efficiency in seven centrality bins.

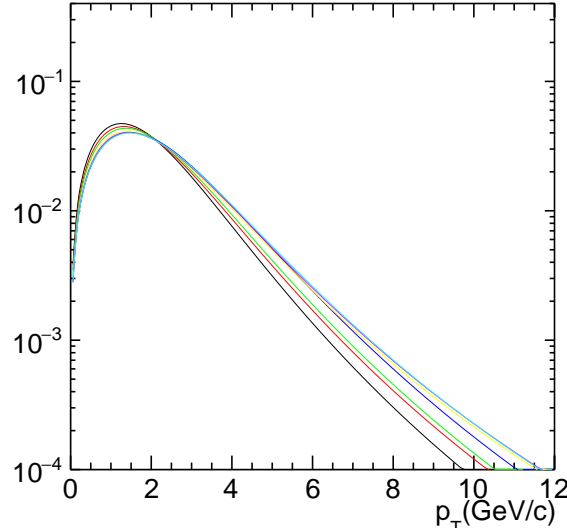


Fig. 17: J/ ψ p_T -differential spectra, corrected by the acceptance \times efficiency in seven centrality bins (color of the lines correspond to the ones shown in Fig. 16).

the acc. \times eff. up to 4%. A smooth distribution (obtained applying TH1D::Smooth()) has been used (as shown in Fig. 18), in the analysis, to evaluate the final acc. \times eff. Furthermore, an interpolation of the values is adopted, when a different binning is applied. Since the weighting procedure is applied only to one bin (60-90%), in order to extract the acc. \times eff. values in 60-70%, 70-80% and 80-90%, the relative difference between the acc \times eff in 60-90% and in the narrower bins, evaluated in the standard embedding MC, is applied. It should be pointed out that the acc. \times eff. values in narrower centrality bins (in the range 60-90%) differs from the 60-90% one by 0.1% (e.g. in the standard embedding MC the acceptance time efficiency in 60-70% is 0.14100, in 70-80% is 0.14140, while in 80-90% is 0.14085. The acceptance times efficiency in 60-90% is 0.1416, so the difference is less than 0.5%).

Following the same approach, the acc. \times eff. has also been computed applying the cut $p_T > 0.3$ GeV/c to remove the photo-production contribution.

We have also evaluated the influence of the centrality-dependence of the y shapes on the acc. \times eff. In a similar way as it was done for the p_T spectra, the y shapes have been tuned in the seven centrality bins, but their impact on the acc. \times eff. turns out to be negligible.

For completeness, in Fig. 19 the acc. \times eff. versus p_T is also shown in the two centrality ranges used in this analysis, i.e. 0-90% and 0-20%. The acceptances in the the two centrality ranges differ by 1-2%.

The acc. \times eff. values used in the analysis are reported in the twiki:

285

<https://twiki.cern.ch/twiki/bin/viewauth/ALICE/JPsiPbPb2015Raa>

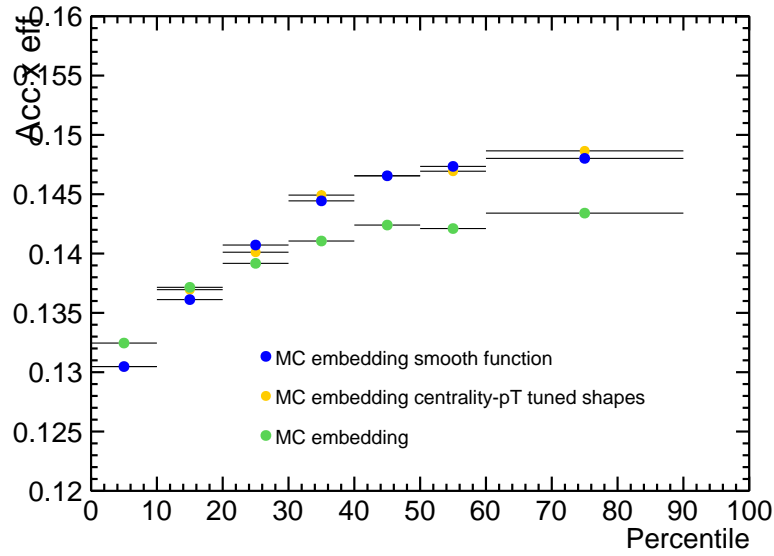


Fig. 18: comparison of the acc. \times eff. values obtained with and without applying the weight to account for the centrality dependence of the J/ψ input shapes. A smooth distribution corresponding to the weighted acc. \times eff. is shown.

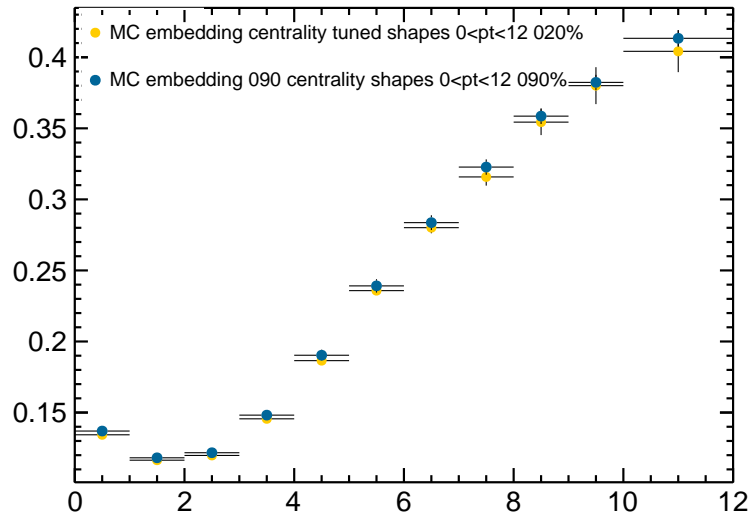


Fig. 19: Acc. \times eff. values versus p_T in the centrality range 0–90% and 0–20%.

6 Systematic uncertainties on MC inputs

As discussed in Section 5, the MC embedding used in this analysis has been corrected to account for the centrality dependence of the p_T J/ ψ input shapes. However, following this approach, we neglect possible p_T - y correlations which might be present. To investigate this issue, we have followed an alternative method. We have extracted the number of J/ ψ in a 3D-approach, i.e. in 7 centrality bins, 4 p_T bins and 3 y bins, corresponding to a total of 84 bins. In order to account simultaneously for the p_T - y correlation and for the centrality-dependence of the J/ ψ kinematic shapes, the $\text{Acc.} \times \text{eff.}$ from MC embedding has been weighted by the number of reconstructed J/ ψ in each p_T - y -centrality bin, using Eq. 12:

$$(\text{Acc} \times \text{eff})_i = \frac{\sum_{p_T, y} (\text{Acc} \times \text{eff})_{i, p_T, y}^{0-90\%} \times N_i^{J/\psi}(p_T, y)}{\sum_{p_T, y} N_i^{J/\psi}(p_T, y)} \quad (12)$$

where $(\text{Acc} \times \text{eff})_{i, p_T}^{0-90\%}$ is the acceptance computed, in bins of p_T and y , using as input the shapes tuned on data in 0-90%.

The resulting $\text{acc.} \times \text{eff.}$ is shown in Fig. 20 (left). The values are very similar to the one discussed in Sec. 5, obtained using as weight the p_T J/ ψ differential shapes, but with larger uncertainties, driven by the limited J/ ψ statistics. The comparison of the resulting $\text{acc.} \times \text{eff.}$ obtained with the two different weights provides the size of the systematic uncertainty associated to p_T - y correlations. As shown in Fig. 20 (right), the size of this systematic uncertainty amounts to 2%. This value is obtained from the average difference between the two approaches ($\sim 1\%$), obtained fitting the distribution in Fig. 20 (right), and its RMS ($\sim 0.7\%$). (blue band in Fig. 20 right).

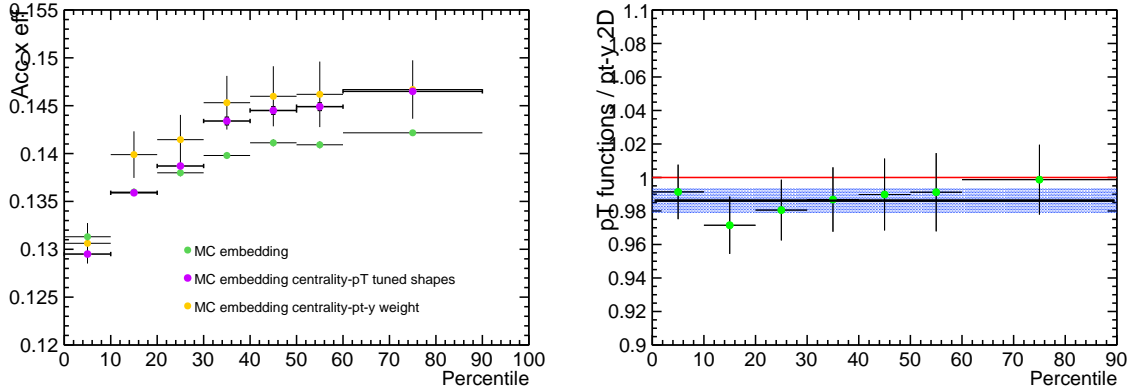


Fig. 20: Left: comparison of the embedding $\text{acc.} \times \text{eff.}$ obtained without applying weights (green symbols), using, as weights, the J/ ψ number extracted in p_T - y -centrality (yellow symbols) or using, as weights, the J/ ψ p_T distributions in centrality bins. Right: ratio of the $\text{acc.} \times \text{eff.}$ obtained with the two different weights, providing the systematic uncertainty due to the p_T - y correlation.

A further contribution to the systematic uncertainty on the MC inputs is due to the statistical uncertainty on the J/ ψ values, as a function of p_T , fitted to extract the distributions used as weights. This uncertainty has been evaluated with a toy-MC, allowing the experimental data points to fluctuate, following a gaussian distribution, within their statistical uncertainties. For each “new” set of data, obtained moving the data points within their statistical uncertainties, a fit to the J/ ψ p_T distribution is performed and the resulting functions are used as weight for the $\text{acc} \times \text{eff.}$ The procedure has been repeated 1000 times for each centrality class. The RMS of the $\text{acc.} \times \text{eff.}$ distribution provide the systematic uncertainty which is smaller than 0.5% in all centrality bins (see Fig. 21). All in all the uncertainty associated to the MC input is obtained summing in quadrature the two contributions and it amounts to 2%, with a negligible dependence on the centrality of the collisions.

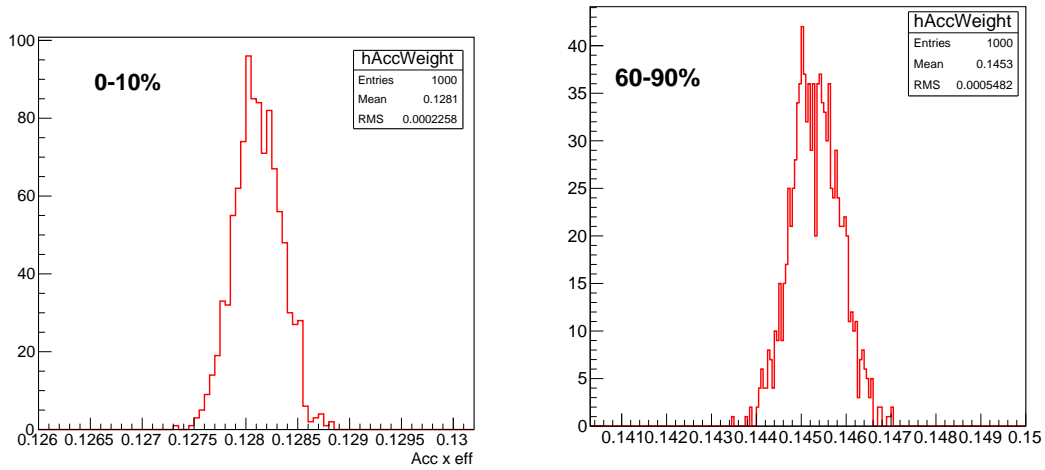


Fig. 21: Acc. \times eff. distributions obtained varying the experimental data points within the statistical uncertainties. Plots refer to 0-10% on the left and 60-90% on the right.

The systematic uncertainty on the MC input is considered as correlated versus centrality, but uncorrelated vs rapidity or transverse momentum.

7 Systematic uncertainties on tracking efficiencies

7.1 Introduction

First of all, the agreement between data and MC is improved by comparing cluster maps, looking for malfunctioning or dead areas not reproduced in the status map, which already compiles the detector status during data taking (HV, pedestal,...). These problematic areas are included in the reject list applied during both data and MC reconstructions. This work has been done before the Pb-Pb data taking period. An example of cluster map for chamber 9, where an extra dead area is spotted, is shown on Figure 22.

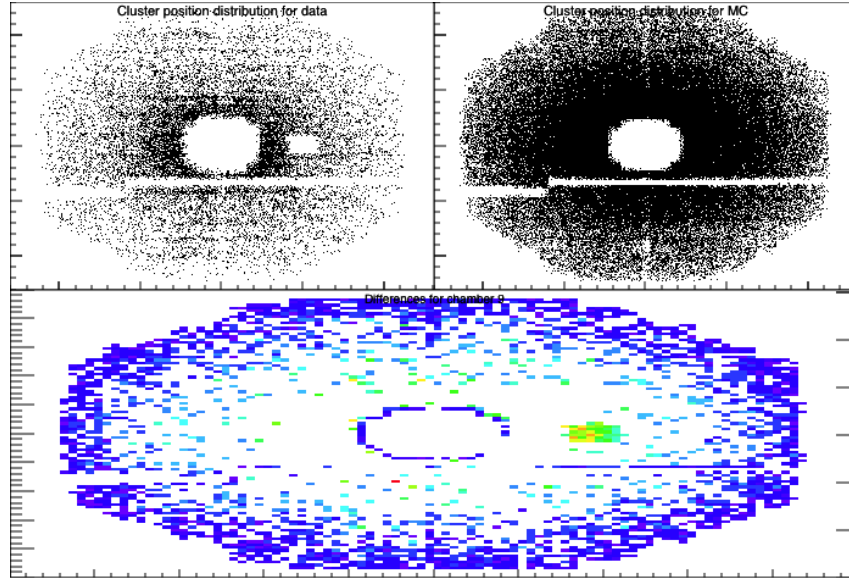


Fig. 22: Clusters maps of chamber 9 from data and MC.

The residual disagreement between data and MC is then assessed by measuring the tracking efficiency. The tracking algorithm used to compute the tracking efficiency is the same as in 2011 studies [3]. It is based on the redundancy of the tracking chambers. This redundancy of the tracking chambers is used to measure their individual efficiencies using the reconstructed tracks. Since such efficiencies are independent from each other, one can combine them to assess the overall tracking efficiency. This method is not precise enough to directly correct the data and only the mean efficiency per chamber can be computed with the statistics available in each run. Since the efficiency of a given chamber is not constant across the whole detection area, it also means that this measurement depends on the distribution of the muons used to perform it. Nevertheless, by comparing the results obtained from data with the same measurement performed in simulations with similar distribution of muons, the accuracy of these simulations is controlled and we assess the corresponding systematic uncertainty on the AccxEff corrections. This work has been done for single muons. We assume the relative tracking systematics for the J/ψ to be twice the value found for the single muons.

7.2 Data driven method and generated input distributions

Prior to compute the tracking efficiency, one should make sure that the generated muon distributions used in simulations (Gen_{MC}) are similar to the real ones ($Corr_{Data}$), and correlatively that the reconstructed muon distributions in simulations (Rec_{MC}) are also similar to the ones in data (Rec_{Data}). A difficulty occurs as we do not know a priori the real muon p_T and y distributions and we only have access to the reconstructed ones. To overpass this problem, a data-driven method has been used. The procedure is as follow:

1. Run some initial simulations with realistic ad hoc input distributions.
2. Compute the acceptance x efficiency AccxEff_{MC} as a function of p_T and y , defined as the ratio of the Rec_{MC} over the Gen_{MC} distributions.
3. Use AccxEff_{MC} to correct the reconstructed muon distributions in data and get Corr_{Data} .
4. Correct the generated distributions in simulations to match Corr_{Data} by weighting each track based on the ratio of new input shapes fitted to Corr_{Data} over the initial shapes used at step 1. A weighing is also applied on a run-by-run basis to match the relative number of events used in each run between data and MC.
5. Repeat step 2 to 4 until the ratios of the Corr_{Data} over Gen_{MC} p_T and y distributions converge to 1.
6. Run new simulations with the tuned input distributions that can now be used to perform tracking efficiency studies.

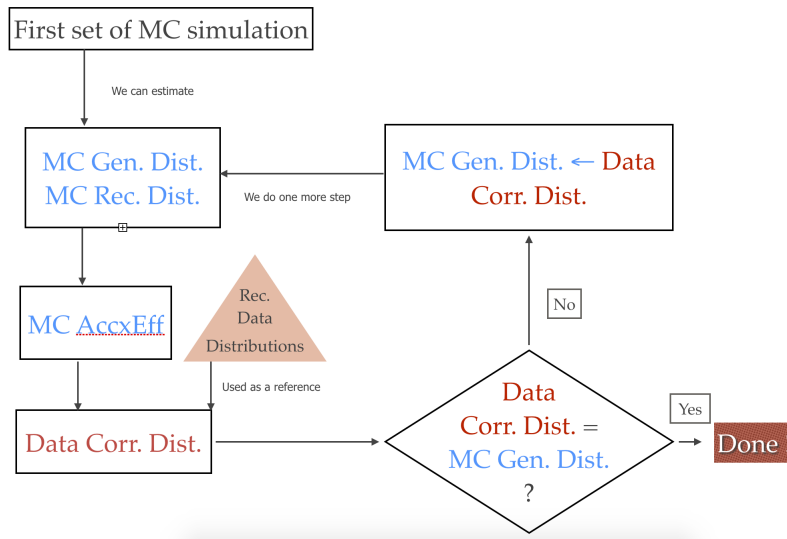


Fig. 23: Illustration of the data driven method used to tune the input distributions in simulations to match the data.

A small illustration of the procedure is given in Figure 23. Note that this tuning has been done looking only at the p_T and y distributions, assuming a flat distribution in ϕ . Standard track cuts are applied both in data and simulations, including the pDCA cut to reject as much as possible tracks not coming from the vertex in data, like secondaries produced in the front absorber or fake tracks, as they cannot be reproduced in pure muon simulations. Events in data are selected in the centrality range 50-90% where the tracking efficiency is not affected by the detector occupancy (see section 7.4), and physics selection is applied. In order to check the stability of the systematic uncertainty evaluation with respect to the distributions of muons used for efficiency measurements, three simulations with three different tuning have been performed based on muon distributions from CMUL7, CMSL7 and CMSH7 triggered events. Each simulation is compared to the corresponding data sample for systematic uncertainty evaluation. A minimum p_T cut, corresponding to the trigger p_T threshold (1 GeV/c, 1 GeV/c and 4 GeV/c, respectively), is also applied to the reconstructed muons to improve the matching between MC and data distributions.

Results of the tuning based on CMSL7 triggered events are shown in Figure 24. The procedure converges after 3-4 loops and a good agreement is observed for p_T and y distributions, while we see an oscillation in the ϕ distribution ratios. This oscillation has already been significantly reduced by correcting for the

370 global misalignment between the ITS and the spectrometer, which was biasing the determination of the muon kinematics at the vertex position. The remaining discrepancy observed here certainly comes from residual background tracks in the data, like secondaries, which are not reproduced in simulations. It disappears when applying an higher p_T cut to the reconstructed muons.

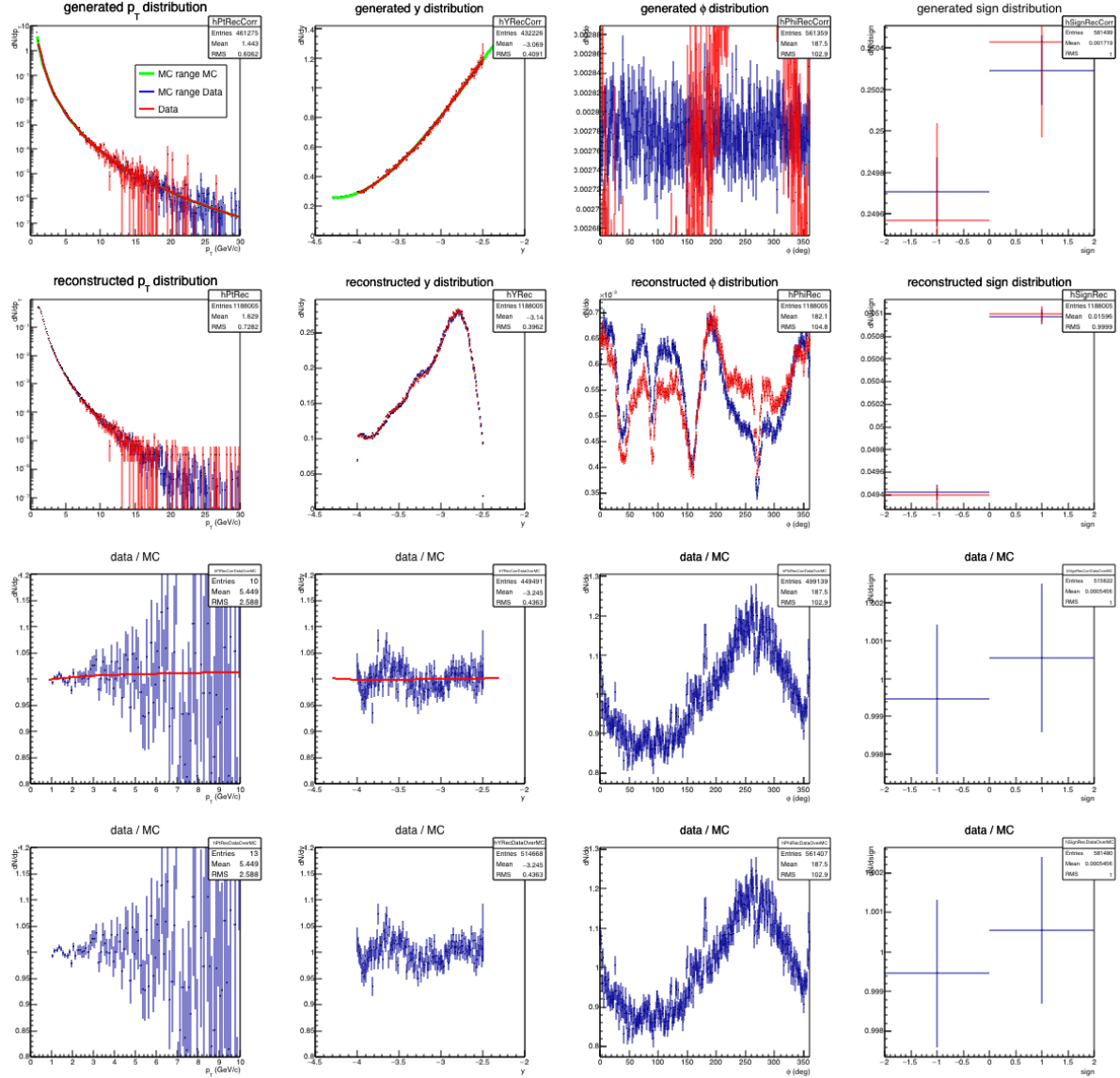


Fig. 24: Comparison of the tuned MC with the reference data from CMSL7 triggered events. Top plots show the comparison of generated (first row) and reconstructed (second row) muon kinematics distributions and bottom plots show the corresponding ratios. The parameterizations of the input shapes used in simulations are $f(p_T) = p_0 \left(\frac{1}{(p_1 + p_T)^{p_3}} + p_4 e^{(p_5 p_T)} \right)$ and $f(y) = p_0 (1 + p_1 y^2 + p_2 y^4)$

7.3 Results

375 Tracking efficiency measurements in CMSL7 triggered data and corresponding tuned MC are shown in Figure 25 as a function of run number, p_T , y and ϕ . Differences between data and MC tend to slightly increase with run as the efficiency decreases. Integrated over the full period, they vary from 0 to $\sim 3\%$ depending on the muon kinematics. In order to check the stability of these results with respect to the

muon distributions and to the quality of the tuning, these measurements are repeated separating μ^+ and μ^- , applying different p_T cuts or varying the centrality range in data. The results are shown in Figure 26. Same studies have been performed with CMUL7 and CMSH7 triggered events and corresponding tuned MC. More details can be found in [4]. A 1.5% systematics uncertainty is observed in average for single muons, with variations depending on the kinematics, the maximum being always with 2-3 σ . This results in a 3% systematics uncertainty for J/ ψ , considered as fully correlated as a function of centrality but not as a function of p_T and y .

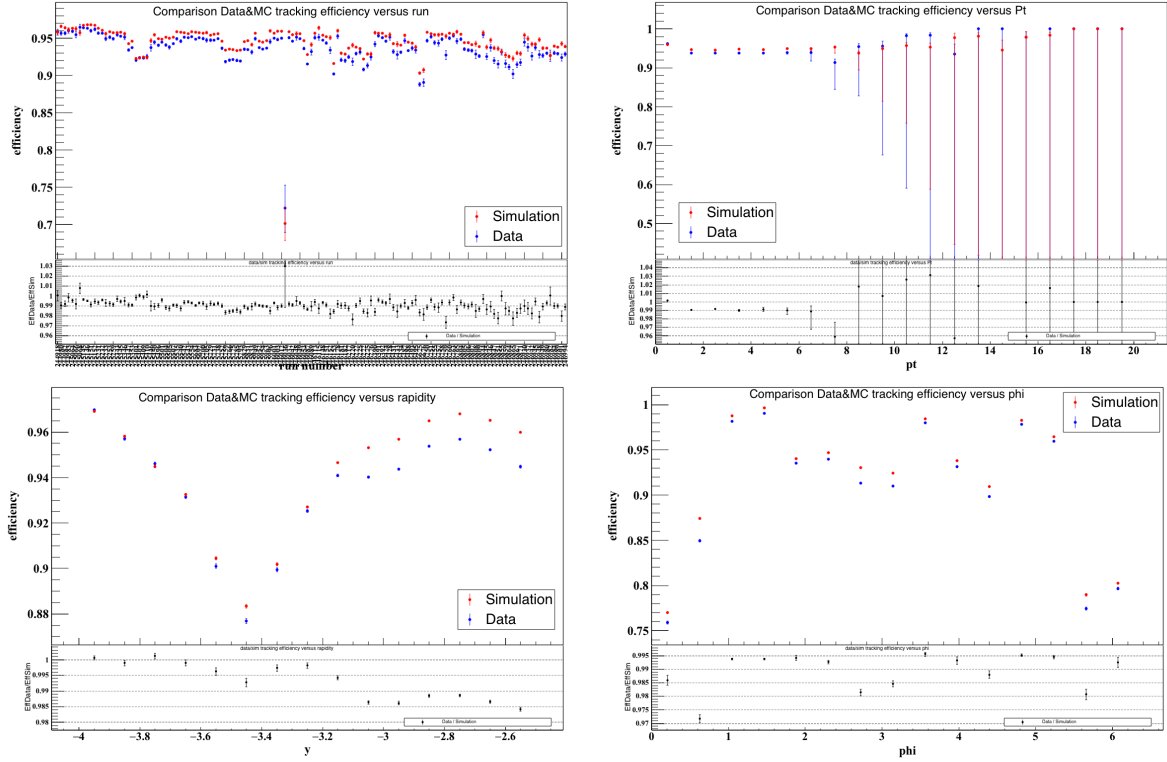


Fig. 25: Tracking efficiency measurement in CMSL7 triggered data and corresponding tuned MC as a function of run number, p_T , y and ϕ .

7.4 Centrality dependent systematic uncertainties

Another source of uncertainty comes from the loss of tracking efficiency with increasing collision centrality, as the detector occupancy increases. This loss of efficiency is reproduced by embedding simulated J/ ψ into real events, and the corresponding systematics uncertainty evaluation is done by measuring the efficiency as a function of centrality in data and comparing the results with the same measurement performed in these simulations. The kinematic distribution of muons between real data and embedding simulations is quite different. However, it has been checked that the differences in the measured efficiency drop with centrality little depend on the muon kinematics. The centrality dependence of the measured tracking efficiencies in CMSL7, CMUU7 and CMSH7 triggered events with different p_T cuts, and in embedding simulations with the same run weightings and p_T cuts are shown in Figure 27. The differences in the efficiency drop between data and MC amount to $\sim 0.5\%$ in most central collisions, which results in a systematic uncertainty of $\sim 1\%$ for J/ ψ . This uncertainty decreases with decreasing centrality, down to 0 in peripheral events, and is considered as fully correlated as a function of p_T and y .

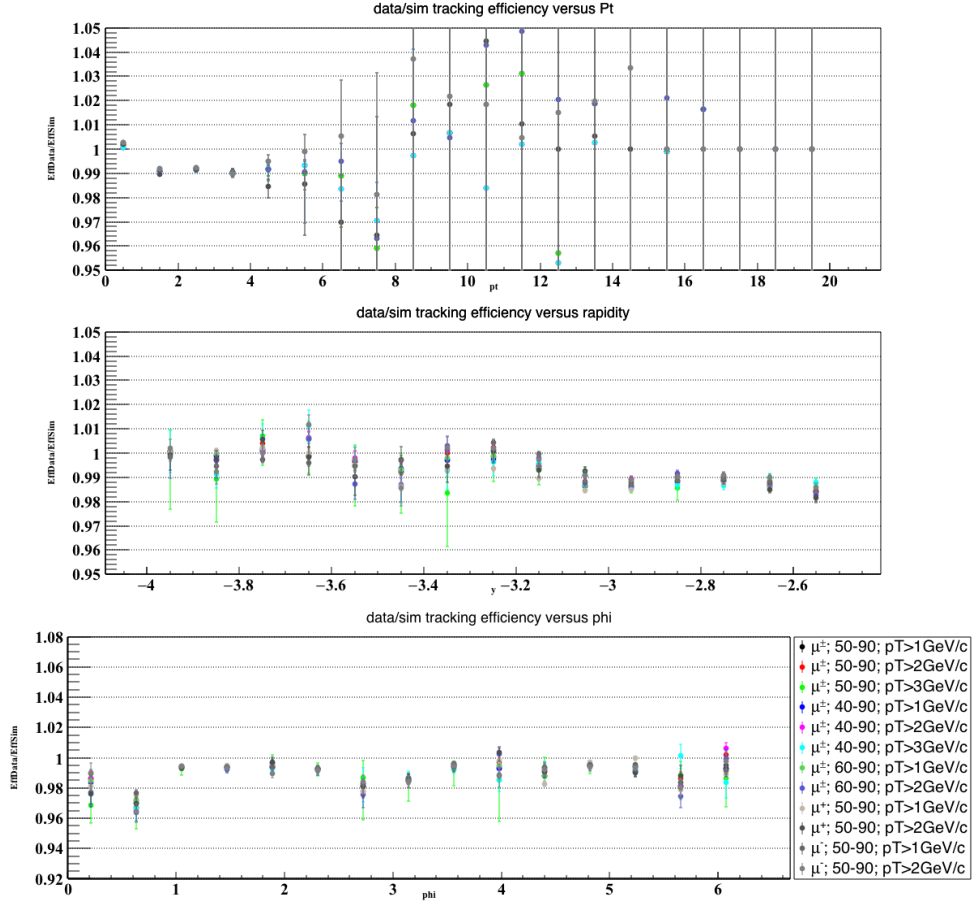


Fig. 26: CMSL7 data over MC tracking efficiency ratios with different event and track selections.

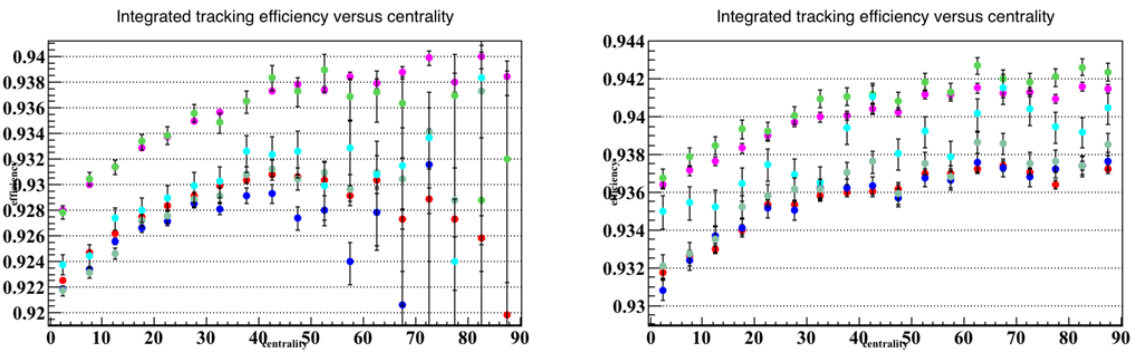


Fig. 27: Tracking efficiency measurements as a function of centrality in CMSL7, CMU7 or CMSH7 triggered events with different p_T cuts (left), and in embedding simulations with the same run weightings and cuts (right).

8 Systematic uncertainties on trigger efficiencies

Two contributions have been considered in the evaluation of the systematic uncertainty on trigger efficiency: first, the difference in the shape of the trigger response distributions in data and MC; second, the uncertainty on the intrinsic trigger chamber efficiency.

8.1 Systematic due to the trigger response distributions

The systematic uncertainty on the shape of the trigger response has been determined by comparing the influence of two different trigger response distributions, obtained in data and in MC, on the $A \times \varepsilon$ of J/ψ . The trigger response distributions have been obtained from the ratio of the Lpt (i.e. 1 GeV/c p_T threshold, used in this analysis) and Allpt (i.e. 0.5 GeV/c p_T threshold) single muon p_T distributions. For the experimental data, single muons from LHC15o period which pass the physics selection, the CINT7-B-NOPF-MUFAST trigger and the pDCA cut have been selected, while for the embedding MC, muons from J/ψ decay have been used. If the pdca cut is not applied, a decrease of the trigger response is observed at high p_T . This decrease is due to the presence of residual background which is still present even if the matching between trigger and tracking is required. The pdca cut, in fact, mainly removes fake tracks, not coming from the vertex, for which the matching is fortuitous and the trigger response is meaningless.

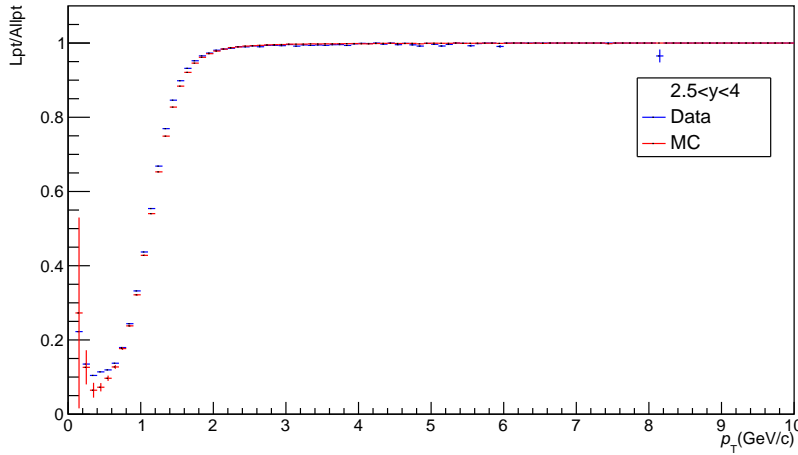


Fig. 28: Lpt/Allpt vs p_T of single muons integrated over y ($2.5 < y < 4.0$).

The data and MC trigger response distributions (Lpt/Allpt) are shown in Fig. 28 for $2.5 < y < 4$ and in three y bins in fig. 29. Trigger response has been measured in rapidity bins to check if there is any rapidity dependence and the fig. 29 shows that there is indeed a rapidity dependence.

The ratio of the data and MC trigger responses, in all the rapidity bins under study, is shown in Fig. 30. Muons coming from the MC J/ψ decay, obtained without applying any trigger request, were weighted according to their kinematics with the two different trigger response distributions, i.e. the one from MC and the one from data. Two different weighting have been tested : 1) using Lpt/Allpt distribution of integrated rapidity ($2.5 < y < 4.0$) and 2) using Lpt/Allpt distributions of three y bins in total to have integrated rapidity range.

The J/ψ acceptance \times efficiency have then been computed starting from the two response functions, one from data and another from MC. The ratio of the resulting $\text{Acc} \times \text{eff.}$ provides the systematic uncertainty on the trigger efficiencies, as shown in Fig. 31. Applying the two weighting approaches, we end up with systematic uncertainties which differs by 1-2%. We decide to use the second way of weighting because

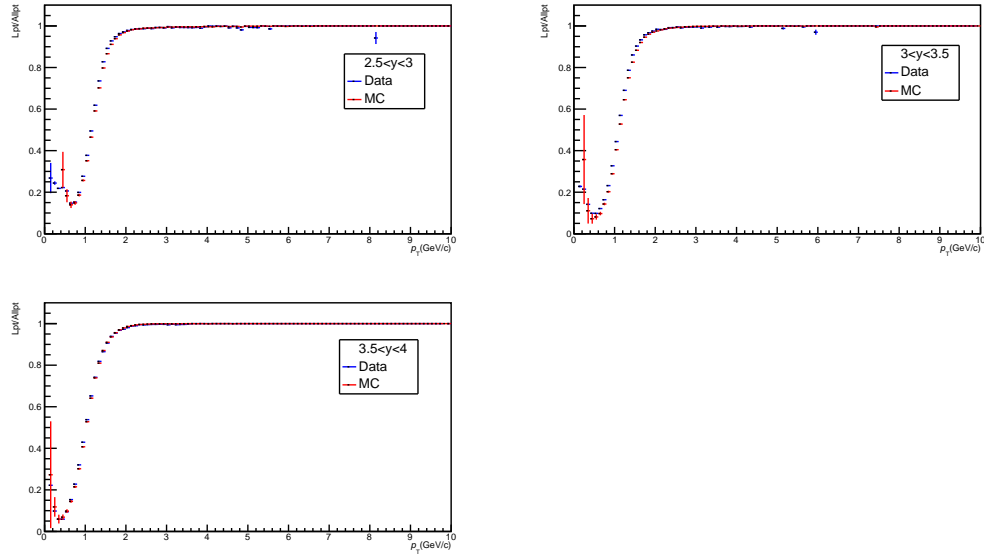


Fig. 29: L_{pt}/All_{pt} vs p_T of single muons in three y bins.

in this way we take into account the y -dependence of the response function.

- 430 The systematic uncertainty, integrated over p_T and y was found to be 3.3%. The systematic uncertainty on the trigger efficiency as a function of p_T and y is bin to bin uncorrelated and it amounts to a maximum 4.6% (taking the max. discrepancy) in the p_T range from 0 to 1 GeV/c. As a function of y , the maximum systematic uncertainty is 4.1% in $2.75 < y < 3$ bin. The table 6 and 7 show the values of the uncertainties in p_T and y bins, respectively.

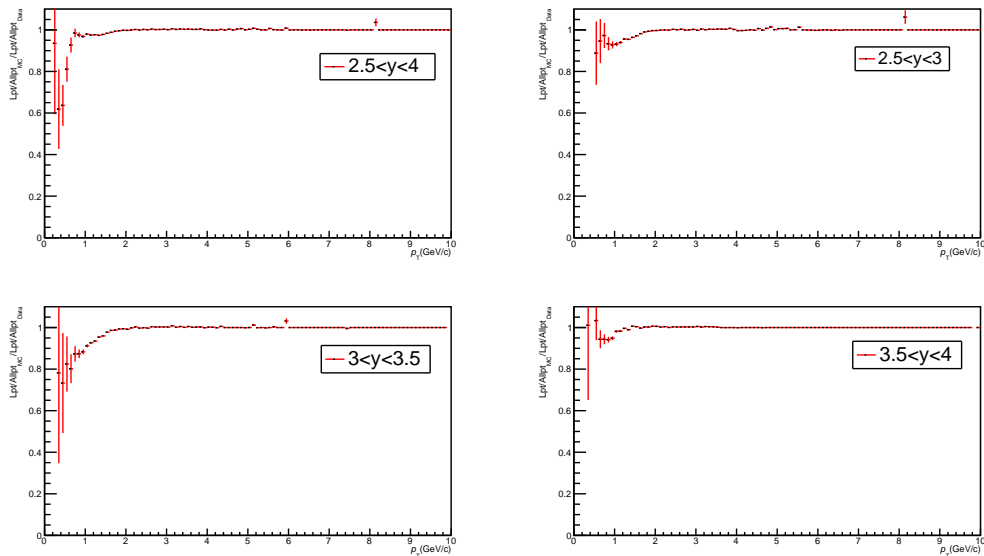


Fig. 30: Ratio of the L_{pt}/All_{pt} vs p_T trigger responses in MC and in data in the rapidity bins under study.

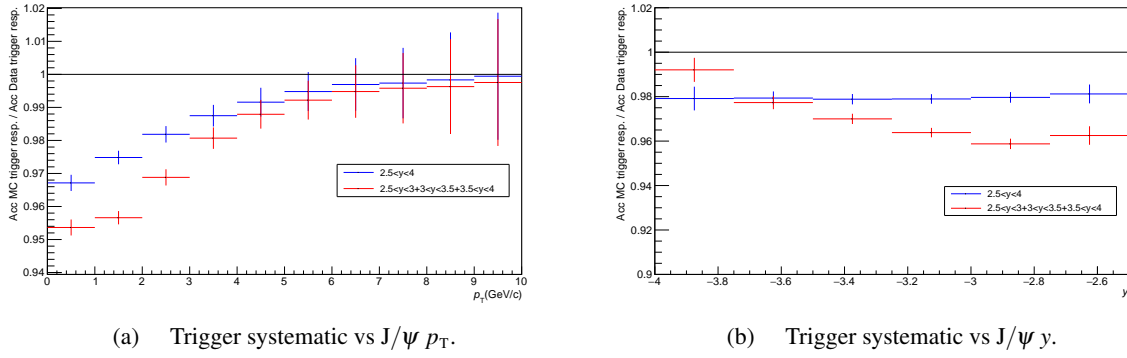


Fig. 31: Ratio of the J/ψ acceptance \times efficiency obtained using the trigger response function from data and from MC. This ratio provides the size of the systematic uncertainty.

p_T bins	Using one response distribution	Using three response distributions
[0; 1]	0.0329	0.0464
[1; 2]	0.0252	0.0434
[2; 3]	0.0182	0.0312
[3; 4]	0.0125	0.0193
[4; 5]	0.0084	0.0121
[5; 6]	0.0052	0.0078
[6; 7]	0.0031	0.0052
[7; 8]	0.0026	0.0042
[8; 9]	0.0017	0.0037
[9; 10]	0.0006	0.0025

Table 6: Relative systematic uncertainties in J/ψ p_T bins.

y bins	Using one response distribution	Using three response distributions
[2.5; 2.75]	0.0188	0.0375
[2.75; 3.0]	0.0203	0.0413
[3.0; 3.25]	0.0210	0.0362
[3.25; 3.5]	0.0211	0.0300
[3.5; 3.75]	0.0206	0.0227
[3.75; 4.0]	0.0209	0.0079

Table 7: Relative systematic uncertainties in J/ψ y bins.

8.2 Systematic due to the intrinsic trigger efficiency

The systematic uncertainty arising from the intrinsic trigger efficiency was estimated by varying, in the simulation, the efficiency of each local board by its uncertainty. The uncertainty on the trigger efficiency has been evaluated comparing the efficiencies obtained in different trigger classes and with different methods and details can be found in

https://indico.cern.ch/event/482176/contributions/2000604/attachments/1218555/1780620/mtrChEff_2015.pdf

For almost all the local boards the uncertainty on the trigger efficiency turns out to be 1.5%, but for some local boards the variations are much larger: 10% for the non-bending planes of the local boards 26 and

30, 5% for the bending planes of the local boards 26 and 30 and 5% for the non-bending planes of 27-29
 445 local boards of Chamber 11, and 10% for the non-bending planes of 68 and 69 boards of Chamber 14.
 A pure J/ ψ MC sample has, therefore, been simulated, by decreasing the trigger efficiencies by their
 uncertainties, local board by local board. Comparing the J/ ψ acceptance \times efficiency obtained in this
 MC with the acceptance \times efficiency evaluated in a pure J/ ψ signal simulation based on the default
 trigger efficiencies, a systematic uncertainty on the of the order of 1.5% is estimated. This systematic
 450 uncertainty, evaluated as a function of p_T and y bins, are also shown in fig. 32. A 0th order polynomial
 fit shows the variation is 1.5% for both p_T and y bins.

The two systematics mentioned above are to be added in quadrature to have the final systematic on trigger
 efficiency.

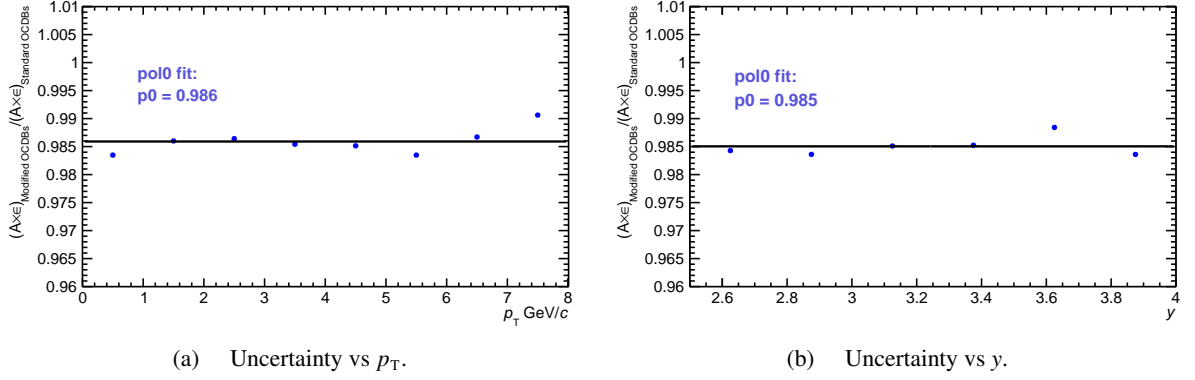


Fig. 32: Systematic due to the intrinsic trigger efficiency, obtained using the standard and the modified OCDB.

9 Summary of systematic uncertainties

9.1 Systematic uncertainty on $\langle T_{AA} \rangle$

The values of $\langle T_{AA} \rangle$ used in this analysis were obtained via a Glauber calculation [5]. The systematic uncertainty is 3.2% for the 0-90% centrality range and was obtained varying, within uncertainties, the density parameters of the Pb nucleus and the nucleon-nucleon inelastic cross section.

9.2 Systematic uncertainty on the centrality limits

The effects of the uncertainty on the value of the V0 signal amplitude corresponding to 90% of the hadronic Pb–Pb cross section were estimated by varying such a value by $\pm 0.5\%$ and redefining correspondingly the centrality intervals. The choice of the 0.5% value has two contributions: i) the sensitivity to the fitting range of the V0 spectrum, chosen to define the 90% anchor point, ii) the sensitivity to the Glauber parameters used in such a fit.

In order to evaluate the influence of the 0.5% shift on the centrality limits, the R_{AA} has been computed using as percentile estimators, the so-called VOM (default estimator) and the equivalent ones shifted by $\pm 0.5\%$, i.e. VOMplus and VOMminus. The systematic uncertainty on R_{AA} is completely dominated by the uncertainty due to the number of J/ψ since the other terms, as, for example, the variation on the acceptance, due to the choice of the VOM, VOMplus or VOMminus is negligible ($\sim 0.1\%$). Therefore the uncertainty on R_{AA} coincide with the uncertainty on the number of J/ψ . As shown in Fig. 33, the

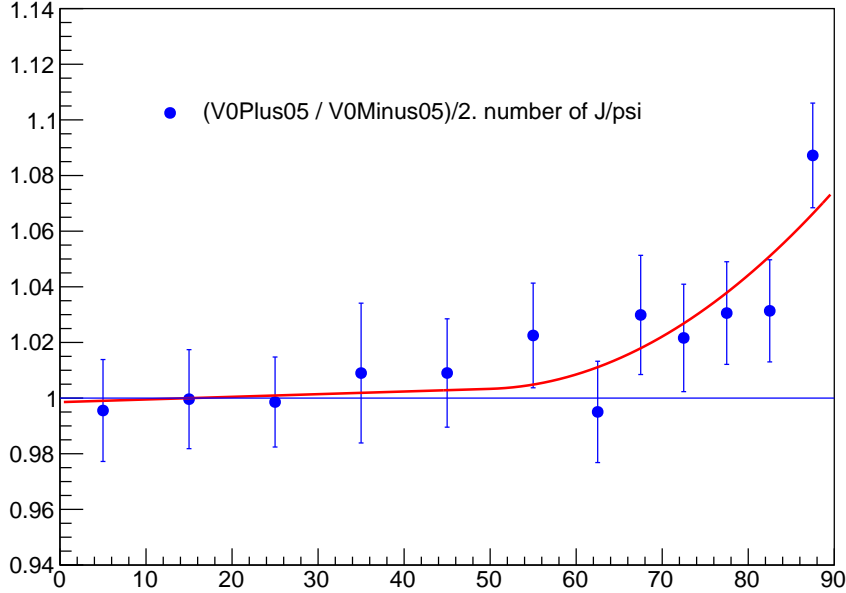


Fig. 33: Systematic uncertainty due to the choice of the centrality limits as a function of centrality

uncertainty on the centrality limits is evaluated from the ratio of the number of J/ψ extracted in VOMplus and VOMminus in each centrality bin. A fit to the resulting distribution is, then, performed, in order to evaluate this systematic uncertainty as a function of the centrality binning chosen for the analysis. The systematic uncertainty on R_{AA} ranges from 0.1% to 6.6% from central to peripheral collisions.

9.3 Summary of systematic uncertainties

Finally, all the systematic uncertainties used in this analysis, concerning both the R_{AA} evaluation and the pp J/ψ cross section, are summarized in Table 9.3.

Source	R_{AA}			$d^2\sigma_{J/\psi}^{pp}/dydp_T$	
	0–90% $p_T < 12$ GeV/c	vs p_T (0–20%)	vs centrality ($p_T < 8$ GeV/c)	$p_T < 12$ GeV/c	vs p_T
Signal extr.	1.8	1.2–3.1	1.6–2.8	3	1.5–9.3
MC input	2	2	2*	2	0.7–1.5
Tracking eff.	3	3	3*	1	1
Trigger eff.	3.6	1.5–4.8	3.6*	1.8	1.5–1.8
Matching eff.	1	1	1*	1	1
$F(L_{int}^{pp})$	0.5	0.5*	0.5*	(2.1)	(2.1*)
BR	-	-	-	0.5	0.5*
$\langle T_{AA} \rangle$	3.2	3.2*	3.1–7.6		
Centrality	0	0.1*	0–6.6		
pp reference	4.9	$3-10 \oplus 2.1^*(L_{int}^{pp})$	5.2*		

Table 8: Summary of systematic uncertainties, in percentage, on R_{AA} and $d^2\sigma_{J/\psi}^{pp}/dydp_T$. Values marked with an asterisk correspond to correlated uncertainties as a function of p_T (second and fifth column) or centrality (third column). There is no correlation between the uncertainties related to the analysis of the Pb-Pb and of the pp sample. The contents of the “pp reference” row correspond to the quadratic sum of the contributions indicated for $d^2\sigma_{J/\psi}^{pp}/dydp_T$, excluding only the BR uncertainty which cancels out when forming the R_{AA} .

10 Results

The modification of the J/ψ production in Pb-Pb collisions is estimated through the nuclear modification factor R_{AA} defined, in a given p_T and centrality class i as:

$$R_{AA}^i(\Delta p_T) = \frac{N_{J/\psi}^i(\Delta p_T)}{(Acc \times eff)^i(\Delta p_T) \cdot N_{MB}^i \cdot T_{AA}^i \cdot \sigma_{J/\psi}^{pp}(\Delta p_T)} \quad (13)$$

where $N_{J/\psi}^i(\Delta p_T)$ is the number of J/ψ , $(Acc \times eff)^i$ is the acceptance and reconstruction efficiency value, T_{AA}^i is the nuclear overlap function and $\sigma_{J/\psi}^{pp}(\Delta p_T)$ is the J/ψ cross section in pp, used here as a reference, evaluated at the same energy and in the same kinematic region of the Pb-Pb values. The $\sigma_{J/\psi}^{pp}$ adopted for the R_{AA} evaluation has been obtained analysing the data at $\sqrt{s}=5\text{TeV}$ that ALICE collected in Fall 2015. Details on the analysis of the pp data can be found in the corresponding analysis note in <https://aliceinfo.cern.ch/Notes/node/500>. In Table 9 and Table 10 the pp cross section values used in the following, for the evaluation of both the R_{AA} as a function of centrality and as a function of p_T are reported.

p_T range	$\sigma_{J/\psi}^{pp} (\mu\text{b})$
$0 < p_T < 8 \text{ GeV/c}$	$5.55 \pm 0.08 \pm 0.27$
$0.3 < p_T < 8 \text{ GeV/c}$	$5.47 \pm 0.08 \pm 0.27$
$0 < p_T < 12 \text{ GeV/c}$	$5.61 \pm 0.08 \pm 0.28$

Table 9: J/ψ cross sections in three transverse momentum ranges

p_T (GeV/c)	$d^2\sigma_{J/\psi}^{pp}/dydp_T$
$0 < p_T < 1$	$0.6509 \pm 0.0238 \pm 0.0331$
$1 < p_T < 2$	$1.1731 \pm 0.0311 \pm 0.0517$
$2 < p_T < 3$	$0.9033 \pm 0.0273 \pm 0.0361$
$3 < p_T < 4$	$0.5192 \pm 0.0193 \pm 0.0213$
$4 < p_T < 5$	$0.2304 \pm 0.0126 \pm 0.0134$
$5 < p_T < 6$	$0.1268 \pm 0.0076 \pm 0.0049$
$6 < p_T < 7$	$0.0621 \pm 0.0051 \pm 0.0022$
$7 < p_T < 8$	$0.0291 \pm 0.0033 \pm 0.0009$
$8 < p_T < 9$	$0.0144 \pm 0.0024 \pm 0.0007$
$9 < p_T < 10$	$0.0112 \pm 0.0020 \pm 0.0011$
$10 < p_T < 12$	$0.0034 \pm 0.0007 \pm 0.00009$

Table 10: $d^2\sigma_{J/\psi}^{pp}/dydp_T$ in the p_T range $0 < p_T < 12 \text{ GeV/c}$. On top of the uncertainties reported in the table, there is a further global uncertainty of 2.16%, containing the BR and the lumi uncertainties contributions.

It has to be pointed out that all the results which have been presented are for inclusive J/ψ production (sum of prompt and non-prompt production). Since beauty hadron decays occur outside the QGP, the non-prompt J/ψ R_{AA} is related to the energy loss of the b-quarks in the medium. The difference between the R_{AA} of prompt and inclusive J/ψ can be estimated using the fraction F_b of non-prompt to inclusive J/ψ in pp collisions, assuming two extreme cases for the R_{AA} of non-prompt J/ψ , namely no medium effects on b-quarks or their complete suppression. F_b was obtained by an extrapolation of the LHCb measurements at $\sqrt{s}=2.76$ and 7 TeV.

The J/ψ R_{AA} integrated in 0-90% centrality at $\sqrt{s_{NN}}=5.02 \text{ TeV}$ is $R_{AA} = 0.66 \pm 0.01(\text{stat}) \pm 0.05(\text{syst})$, for $2.5 < y < 4$ and $p_T < 8 \text{ GeV/c}$. The same quantity at $\sqrt{s_{NN}}=2.76 \text{ TeV}$ was $R_{AA} = 0.58 \pm 0.01(\text{stat}) \pm 0.09(\text{syst})$, lower by about 15%, corresponding to 0.7σ difference.

Since the p_T coverage of the J/ ψ cross sections in pp collisions extends up to 12 GeV/c, we have also computed the inclusive J/ ψ R_{AA} in the range $0 < p_T < 12$ GeV/c. The resulting value is $R_{AA} = 0.65 \pm 0.01(\text{stat}) \pm 0.05(\text{syst})$.

The double ratio between the R_{AA} results at $\sqrt{s_{NN}} = 5.02$ TeV and 2.76 TeV (computed in the common p_T region $0 < p_T < 8$ GeV/c) is $1.13 \pm 0.02 \pm 0.18$. The only contribution to the systematic uncertainty which cancel out in the ratio is the uncertainty on $\langle T_{AA} \rangle$.

In Fig. 34 (left), the R_{AA} has been evaluated as a function of centrality and compared to the R_{AA} results obtained at $\sqrt{s_{NN}} = 2.76$ TeV. The R_{AA} at the two energies differ by 15%, almost independently on the centrality of the collisions. The large sample of data collected in 2015 has allowed us to evaluate the R_{AA} adopting narrow centrality bins, as shown in Fig. 34 (right). No clear structures are visible for $N_{part} > 100$. A zero-order polynomial fit, performed for $N_{part} > 100$, describes the data, with a $\chi^2/ndf = 0.3$. In Table 11 and Table 12 the numerical R_{AA} results are given.

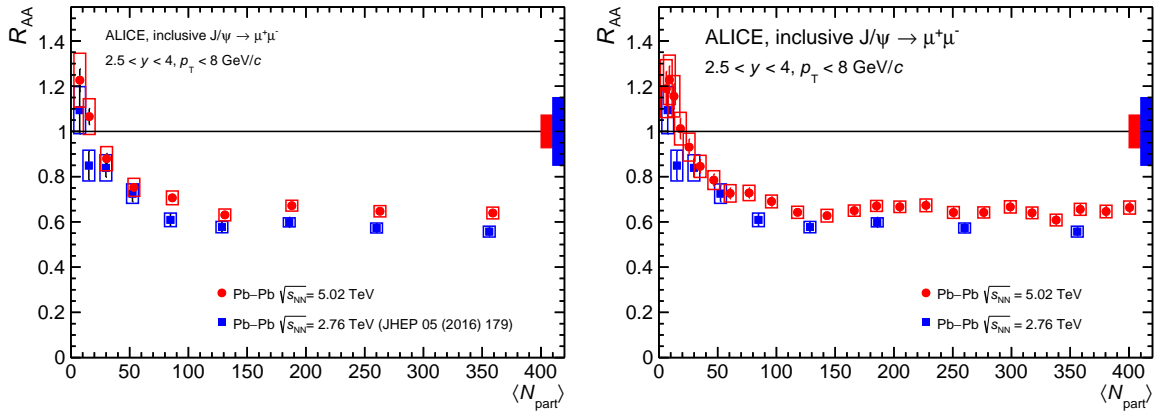


Fig. 34: R_{AA} as a function of centrality measured at $\sqrt{s_{NN}} = 2.76$ (blue symbols) and 5.02 TeV (red symbols). In the left plot, the same centrality binning has been used at both energies, while in the right plot, a finer binning is used for the results at $\sqrt{s_{NN}} = 5.02$ TeV. The width of the centrality classes are, in the latter case, 2% from 0 to 12%, 3% from 12% to 30% and 5% for the most peripheral collisions. Error bars are the statistical uncertainties, while the systematic uncertainties are the boxes around the points. The box at $R_{AA} = 1$ represents the global uncertainty.

In order to reduce the J/ ψ contribution from photo-production, playing a role in peripheral collisions, a cut at the J/ ψ transverse momentum $p_T > 300$ MeV has been applied. The same cut was already used in the 2011 J/ ψ analysis, where its efficiency was $\sim 75\%$. The efficiency of this cut at $\sqrt{s_{NN}} = 5.02$ TeV is 80%. The effect of the cut is visible in Fig. 35.

The hadronic J/ ψ R_{AA} for $0 < p_T < 8$ GeV/c is estimated to be about 34%, 17% and 9% smaller than the measured values in 80-90%, 70-80% and 60-70% centrality classes respectively. The variation decreases to about 9%, 4% and 2%, respectively, when considering the J/ ψ R_{AA} with $0.3 < p_T < 8$ GeV/c. Extreme hypothesis on the amount of photo-produced J/ ψ (assuming 80% in $0 < p_T < 0.3$ GeV/c and 20% in $0.3 < p_T < 8$ GeV/c, as in UPC, or a factor two more in $0.3 < p_T < 8$ GeV/c) were made to define lower and upper limits, represented in Fig. 36 as brackets. The assumptions are the same as those made for the $\sqrt{s_{NN}} = 2.76$ TeV analysis [1].

The R_{AA} of prompt J/ ψ would be about 10% higher if the R_{AA} of non-prompt J/ ψ is zero, and about 5% (1%) smaller if it is equal to 1 for central (peripheral) collisions. Details are given in the Appendix.

Results are compared with theoretical predictions, namely two transport models, an approach based on comover interactions and eventually a statistical hadronization approach, as shown in Fig. 36

The statistical hadronization approach [6] assumes that J/ ψ are fully dissociated in a QGP and produced

centrality (percentile in %)	$J/\psi R_{AA}$
0-2	0.66 +/- 0.02 (stat) +/- 0.03 (syst) +/- 0.05 (global)
2-4	0.65 +/- 0.02 (stat) +/- 0.03 (syst) +/- 0.05 (global)
4-6	0.66 +/- 0.02 (stat) +/- 0.03 (syst) +/- 0.05 (global)
6-8	0.61 +/- 0.02 (stat) +/- 0.03 (syst) +/- 0.04 (global)
8-10	0.64 +/- 0.02 (stat) +/- 0.03 (syst) +/- 0.05 (global)
10-12	0.67 +/- 0.02 (stat) +/- 0.03 (syst) +/- 0.05 (global)
12-15	0.64 +/- 0.02 (stat) +/- 0.02 (syst) +/- 0.05 (global)
15-18	0.64 +/- 0.02 (stat) +/- 0.03 (syst) +/- 0.05 (global)
18-21	0.67 +/- 0.02 (stat) +/- 0.03 (syst) +/- 0.05 (global)
21-24	0.67 +/- 0.02 (stat) +/- 0.03 (syst) +/- 0.05 (global)
24-27	0.67 +/- 0.02 (stat) +/- 0.02 (syst) +/- 0.05 (global)
27-30	0.65 +/- 0.02 (stat) +/- 0.02 (syst) +/- 0.05 (global)
30-35	0.63 +/- 0.02 (stat) +/- 0.03 (syst) +/- 0.05 (global)
35-40	0.64 +/- 0.02 (stat) +/- 0.03 (syst) +/- 0.05 (global)
40-45	0.69 +/- 0.02 (stat) +/- 0.03 (syst) +/- 0.05 (global)
45-50	0.73 +/- 0.02 (stat) +/- 0.03 (syst) +/- 0.05 (global)
50-55	0.73 +/- 0.02 (stat) +/- 0.04 (syst) +/- 0.05 (global)
55-60	0.78 +/- 0.03 (stat) +/- 0.04 (syst) +/- 0.06 (global)
60-65	0.85 +/- 0.03 (stat) +/- 0.05 (syst) +/- 0.06 (global)
65-70	0.93 +/- 0.04 (stat) +/- 0.06 (syst) +/- 0.07 (global)
70-75	1.01 +/- 0.05 (stat) +/- 0.07 (syst) +/- 0.07 (global)
75-80	1.16 +/- 0.06 (stat) +/- 0.09 (syst) +/- 0.08 (global)
80-85	1.23 +/- 0.06 (stat) +/- 0.11 (syst) +/- 0.09 (global)
85-90	1.19 +/- 0.08 (stat) +/- 0.13 (syst) +/- 0.09 (global)

Table 11: $J/\psi R_{AA}$ in narrow centrality bins, for $0 < p_T < 8$ GeV/c.

centrality (percentile in %)	$J/\psi R_{AA}$
0-10	0.63 +/- 0.01 (stat) +/- 0.03 (syst) +/- 0.05 (global)
10-20	0.64 +/- 0.01 (stat) +/- 0.02 (syst) +/- 0.05 (global)
20-30	0.67 +/- 0.01 (stat) +/- 0.02 (syst) +/- 0.05 (global)
30-40	0.62 +/- 0.01 (stat) +/- 0.03 (syst) +/- 0.04 (global)
40-50	0.69 +/- 0.02 (stat) +/- 0.03 (syst) +/- 0.05 (global)
50-60	0.72 +/- 0.02 (stat) +/- 0.04 (syst) +/- 0.05 (global)
60-70	0.81 +/- 0.02 (stat) +/- 0.05 (syst) +/- 0.06 (global)
70-80	0.92 +/- 0.03 (stat) +/- 0.07 (syst) +/- 0.07 (global)
80-90	0.90 +/- 0.04 (stat) +/- 0.09 (syst) +/- 0.07 (global)

Table 12: $J/\psi R_{AA}$ in 10% width centrality bins, for $0.3 < p_T < 8$ GeV/c.

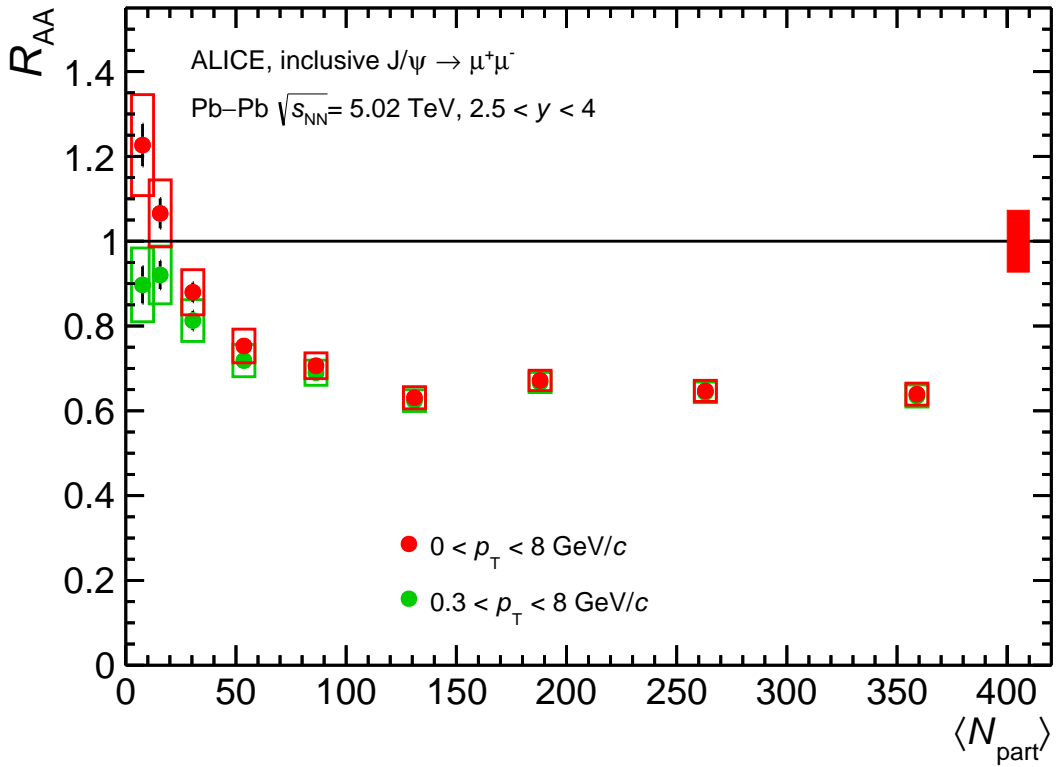


Fig. 35: R_{AA} as a function of centrality measured at $\sqrt{s_{NN}} = 5.02$ TeV with (green symbols) and without (red symbols) the cut on the J/ ψ transverse momentum ($p_T > 300$ MeV/c).

at chemical freeze-out according to their statistical weights. In this model, the nucleon-nucleon open charm cross section is tuned in order to describe the J/ ψ R_{AA} at $\sqrt{s_{NN}} = 2.76$ TeV ($d\sigma_{c\bar{c}}/dy = 0.21$ mb) and then extrapolated to $\sqrt{s_{NN}} = 5.02$ TeV using FONLL, which results in an increase of about 1.59. The uncertainty band associated to this calculation is due to a 20% uncertainty on this cross section.

Transport models [7–9] include continuous J/ ψ regeneration and dissociation in the QGP and in the hadronic phase. In [7, 8], the inclusive open charm cross section is $d\sigma_{c\bar{c}}/dy = 0.57$ mb, and the J/ ψ production cross section value in N-N collisions is $d\sigma_{J/\psi}/dy = 3.14$ μ b. In [9] the used values are $d\sigma_{c\bar{c}}/dy = 0.82$ mb and $d\sigma_{J/\psi}/dy = 3.5$ μ b. In both models the uncertainty band correspond to either no shadowing (upper band) or shadowing (lower band).

Finally a comover model [10] is based on the possibility of dissociating J/ ψ in interactions with the partons/hadrons, with an effective cross section $\sigma_{co-J/\psi} = 0.65$ mb. This value has been tuned on low energy experiments. In this approach, the uncertainty band is associated to the range of variation of $\sigma_{c\bar{c}}$, introduced to account for re-generation effects, ($\sigma_{c\bar{c}} = 0.45$ -0.7 mb). Shadowing effects are also included. They are calculated in a Glauber-Gribov theory and are in agreement with EKS98/nDSg predictions.

As visible in Fig. 36, the agreement between data and the theoretical predictions is rather good, given, however, the large uncertainties associated to the models. In particular, the measured R_{AA} tends to be in better agreement with the upper expectations of the models.

Since the theory models include only the J/ ψ hadronic production, in order to make a meaningful comparison with the experimental results, the cut $p_T > 0.3$ GeV/c is applied to the data. Furthermore, it has been checked, as shown in Fig. 37, that the effect of the p_T cut on theory models is negligible.

Since, at a given extend, some of the input parameters are correlated between $\sqrt{s_{NN}} = 2.76$ and 5.02 TeV,

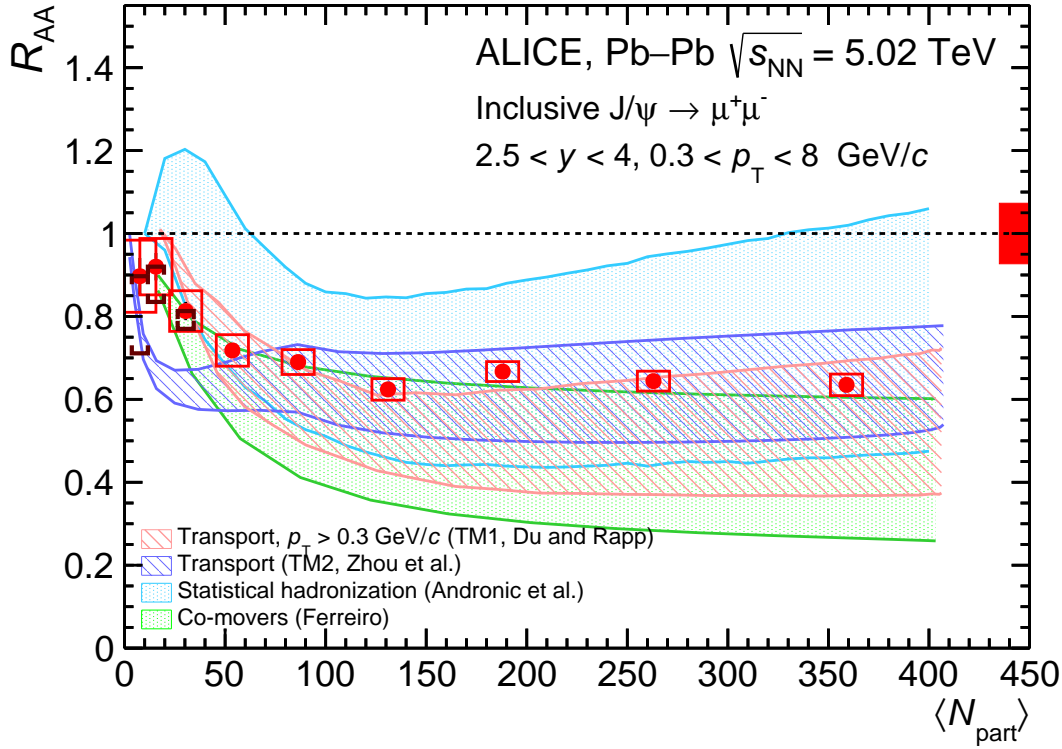


Fig. 36: R_{AA} as a function of centrality measured at $\sqrt{s_{NN}} = 5.02$ TeV (with $0.3 < p_T < 8$ GeV/c) compared to the theory models described in the text. The error bars represent the statistical uncertainties, the boxes around the data points the uncorrelated systematic uncertainties, while the correlated global uncertainty is shown as a filled box around 1. The brackets shown in the three most peripheral centrality intervals represent the range of variation of the hadronic J/ψ R_{AA} under extrem hypothesis on the photo-production contamination of the inclusive R_{AA} .

centrality (percentile in %)	J/ψ double R_{AA} ratio
0-10	1.17 +/- 0.04 (stat) +/- 0.05 (syst) +/- 0.19 (global)
10-20	1.15 +/- 0.04 (stat) +/- 0.03 (syst) +/- 0.19 (global)
20-30	1.12 +/- 0.04 (stat) +/- 0.02 (syst) +/- 0.19 (global)
30-40	1.09 +/- 0.05 (stat) +/- 0.04 (syst) +/- 0.18 (global)
40-50	1.17 +/- 0.06 (stat) +/- 0.04 (syst) +/- 0.19 (global)
50-60	1.00 +/- 0.05 (stat) +/- 0.04 (syst) +/- 0.17 (global)
60-70	1.01 +/- 0.06 (stat) +/- 0.05 (syst) +/- 0.17 (global)
70-80	1.18 +/- 0.10 (stat) +/- 0.07 (syst) +/- 0.20 (global)
80-90	1.01 +/- 0.12 (stat) +/- 0.09 (syst) +/- 0.17 (global)

Table 13: Double ratio of R_{AA} at $\sqrt{s_{NN}} = 5.02$ and 2.76 TeV, in 10% width centrality bins, for $0.3 < p_T < 8$ GeV/c.

it is possible to reduce the uncertainties on the theory calculations when the ratio $r = R_{AA}(5.02 \text{ TeV})/R_{AA}(2.76 \text{ TeV})$ is computed (applying in both cases a p_T cut, $p_T > 0.3$ GeV/c). However, for what concerns the experimental results, almost no systematic uncertainty cancels out, apart from the uncertainty on the evaluation of the $\langle T_{AA} \rangle$. The numerical r values are given in Table 13. The comparison of r with the theory calculations is shown in Fig. 38.

Within the large uncertainties, data are compatible with models, with a hint for r values larger than one over all the centralities. For prompt J/ψ the ratio r would be about 2% (12%) higher if beauty hadrons are fully (not) suppressed by the medium.

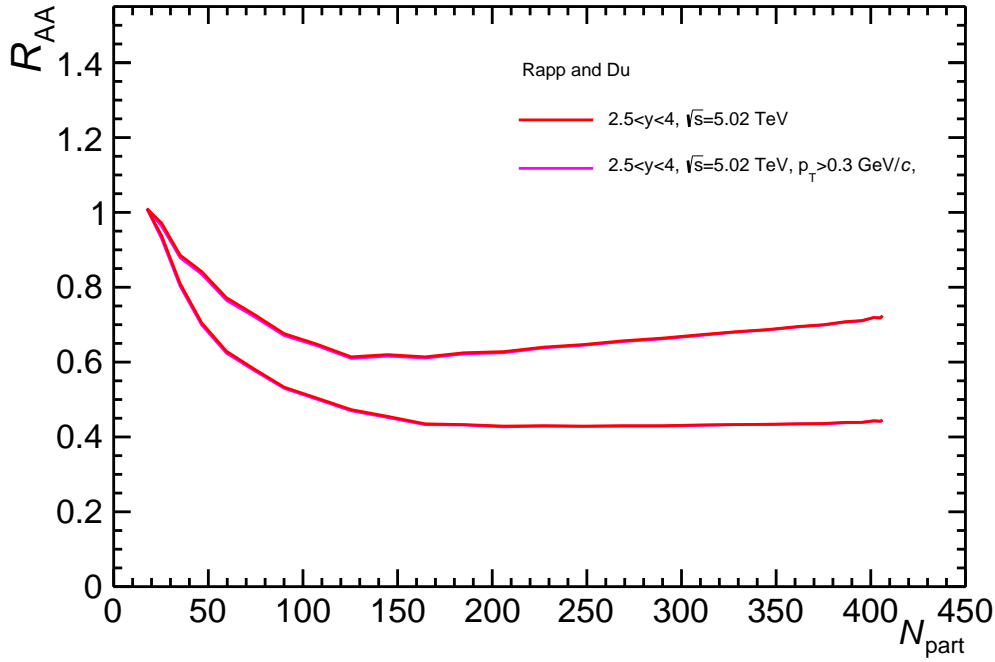


Fig. 37: Theory curves from Rapp's transport model with and without the cut $p_T > 0.3$ GeV/c. It should be noted that these curves do not represent the very final Rapp's prediction, but they are still meaningful to depict the effect of the $p_T > 0.3$ GeV/c cut.

p_T (GeV/c)	J/ ψ R_{AA}
0-1	0.75 +/- 0.03 (stat) +/- 0.07 (syst) +/- 0.03 (global)
1-2	0.73 +/- 0.02 (stat) +/- 0.06 (syst) +/- 0.03 (global)
2-3	0.64 +/- 0.02 (stat) +/- 0.05 (syst) +/- 0.03 (global)
3-4	0.51 +/- 0.01 (stat) +/- 0.04 (syst) +/- 0.02 (global)
4-5	0.47 +/- 0.02 (stat) +/- 0.04 (syst) +/- 0.02 (global)
5-6	0.38 +/- 0.01 (stat) +/- 0.03 (syst) +/- 0.02 (global)
6-7	0.32 +/- 0.01 (stat) +/- 0.03 (syst) +/- 0.01 (global)
7-8	0.30 +/- 0.02 (stat) +/- 0.04 (syst) +/- 0.01 (global)
8-9	0.35 +/- 0.03 (stat) +/- 0.06 (syst) +/- 0.01 (global)
9-10	0.23 +/- 0.03 (stat) +/- 0.05 (syst) +/- 0.01 (global)
10-12	0.35 +/- 0.03 (stat) +/- 0.08 (syst) +/- 0.01 (global)

Table 14: J/ ψ R_{AA} at $\sqrt{s_{NN}} = 5.02$ TeV, as a function of p_T , for 0-20%

Finally, the p_T dependence of the R_{AA} has also been addressed, focussing on the most central events (0-20%). According to (re)combination models, J/ ψ produced by (re)combination should be dominant at low transverse momentum. This behaviour is indeed observed, as it can be noticed comparing the experimental result to the theory prediction of a transport model. Furthermore, as shown in Fig. 39 (left), the R_{AA} at $\sqrt{s_{NN}} = 5.02$ TeV is larger than the one measured at the lower energy.

No p_T cut ($p_T > 0.3$ GeV/c) is applied, since the contribution of photo-produced J/ ψ in the most central collisions is negligible with respect to the hadronic production. The numerical values of the J/ ψ R_{AA} versus p_T are given in Table 14.

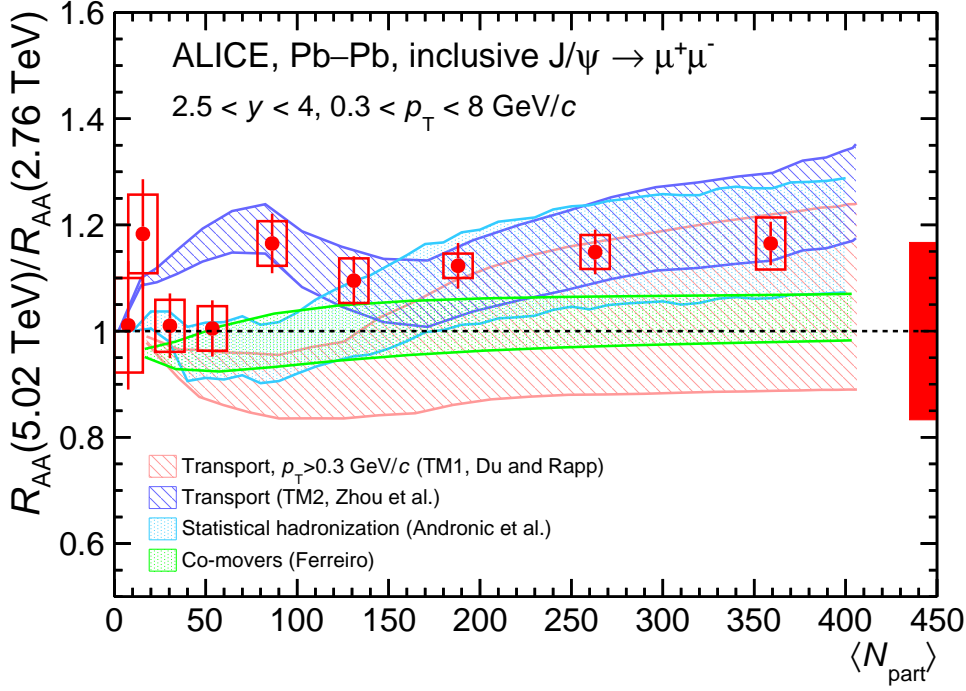


Fig. 38: Comparison of r versus centrality with theory predictions (transport models, statistical hadronization approach and co-movers model)

p_T (GeV/c)	Double ratio of $J/\psi R_{AA}$
0-1	0.93 +/- 0.10 (stat) +/- 0.16 (syst) +/- 0.07 (global)
1-2	1.06 +/- 0.08 (stat) +/- 0.15 (syst) +/- 0.08 (global)
2-3	1.28 +/- 0.11 (stat) +/- 0.18 (syst) +/- 0.10 (global)
3-4	1.34 +/- 0.13 (stat) +/- 0.19 (syst) +/- 0.10 (global)
4-5	1.31 +/- 0.20 (stat) +/- 0.19 (syst) +/- 0.10 (global)
5-6	1.33 +/- 0.23 (stat) +/- 0.19 (syst) +/- 0.10 (global)
6-8	1.12 +/- 0.26 (stat) +/- 0.16 (syst) +/- 0.09 (global)

Table 15: Double ratio of R_{AA} at $\sqrt{s_{NN}} = 5.02$ and 2.76 TeV, as a function of the transverse momentum

The prompt $J/\psi R_{AA} p_T$ dependence is expected to be 7% larger (2% smaller) for $p_T < 1$ GeV/c and 30% larger (55% smaller) for $10 < p_T < 12$ GeV/c when beauty contribution is fully (not) suppressed.

The ratio of the R_{AA} results at $\sqrt{s_{NN}} = 5.02$ and 2.76 TeV is shown in Fig. 39 (top) and the numerical values are given in Table 10. Since the R_{AA} result at $\sqrt{s_{NN}} = 2.76$ TeV extends only up to $p_T = 8$ GeV/c, the same p_T range, and the same p_T binning, is adopted also for the R_{AA} at $\sqrt{s_{NN}} = 5.02$ TeV. The ratio shows $\sim 15\%$ difference between the two measurements in the range $2 < p_T < 6$ GeV/c, while it is consistent with unity elsewhere. The influence of the B feed-down on the double ratio is negligible, in the case of full suppression of beauty hadrons, while it varies from no increase at low transverse momentum up to a maximum increase of about 15% for $5 < p_T < 6$ GeV/c.

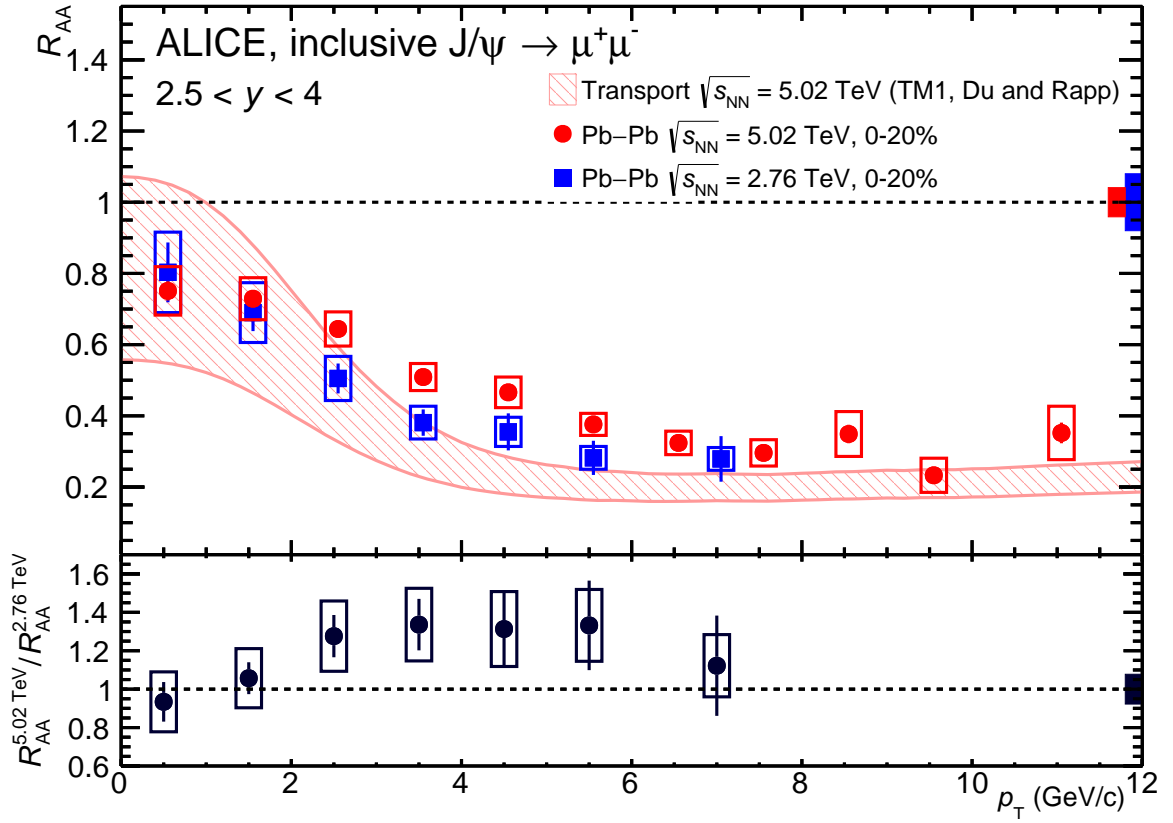


Fig. 39: Top: transverse momentum dependence of R_{AA} both at $\sqrt{s_{NN}} = 2.76$ (blue symbols) and 5.02 TeV (red symbols). The R_{AA} are evaluated for most central collisions (0-20%) and compared to a transport model calculation. Bottom: double ratio as a function of p_T of the R_{AA} measured at $\sqrt{s_{NN}} = 5.02$ TeV and 2,76 TeV

A Fit Functions

Extended Crystal-Ball

575 This function has a normalization factor N , two Gaussian core parameters (\bar{x} and σ) and four tail parameters (α , n , α' and n'). And it is defined by:

$$f(x) = N \cdot \begin{cases} \exp\left(\frac{-(x-\bar{x})^2}{2\sigma^2}\right) & \text{for } \alpha' > \frac{x-\bar{x}}{\sigma} > -\alpha \\ A \cdot \left(B - \frac{x-\bar{x}}{\sigma}\right)^{-n} & \text{for } \frac{x-\bar{x}}{\sigma} \leq -\alpha \\ C \cdot \left(D + \frac{x-\bar{x}}{\sigma}\right)^{-n'} & \text{for } \frac{x-\bar{x}}{\sigma} \geq \alpha' \end{cases}$$

with

$$A = \left(\frac{n}{|\alpha|}\right)^n \cdot \exp\left(-\frac{|\alpha|^2}{2}\right), B = \frac{n}{|\alpha|} - |\alpha|$$

$$C = \left(\frac{n'}{|\alpha'|}\right)^{n'} \cdot \exp\left(-\frac{|\alpha'|^2}{2}\right), D = \frac{n'}{|\alpha'|} - |\alpha'|$$

580 NA60

This function has a normalization factor N , two Gaussian core parameters (\bar{x} and σ) and eight tail parameters (α^L , p_1^L , p_2^L , p_3^L , α^R , p_1^R , p_2^R and p_3^R). And it is defined by:

$$f(x) = N \cdot \exp\left(-0.5 \left(\frac{t}{t_0}\right)^2\right)$$

with

$$t = \frac{x - \bar{x}}{\sigma}$$

and

$$\begin{cases} t_0 = 1 + p_1^L (\alpha^L - t)^{(p_2^L - p_3^L \sqrt{\alpha^L - t})} & \text{for } t < \alpha^L \\ t_0 = 1 & \text{for } \alpha^L < t < \alpha^R \\ t_0 = 1 + p_1^R (t - \alpha^R)^{(p_2^R - p_3^R \sqrt{t - \alpha^R})} & \text{for } t > \alpha^R \end{cases}$$

585 Variable Width Gaussian

This function has a normalization factor N , and four parameters (\bar{x} , α , β , γ), and it is defined by:

$$f(x) = N \cdot \exp\left(\frac{-(x-\bar{x})^2}{2\sigma^2}\right), \text{ where } \sigma = \alpha + \beta \left(\frac{x-\bar{x}}{\bar{x}}\right) + \gamma \left(\frac{x-\bar{x}}{\bar{x}}\right)^2$$

B Effect of non-prompt J/ψ on R_{AA}

At forward rapidity, the muon spectrometer detector is not able to separate J/ψ originating from the decay of B-hadrons (non-prompt component) from those produced either directly or in the decay of charm resonances ($\psi(2S), \chi_c$) (prompt component). Thus the measurements shown in this note always refers to inclusive J/ψ production. Although R_{AA}^{prompt} cannot be directly accessed, it can be evaluated starting from R_{AA}^{incl} , provided hypothesis on (i) the fraction of J/ψ coming from B-hadron decays in pp collisions at $\sqrt{s_{NN}} = 5.02$ TeV, in the kinematic coverage of the muon spectrometer, (ii) the suppression of B-hadron production in Pb-Pb collisions due to initial and final state nuclear effects. As a function of p_T , $R_{AA}^{prompt}(p_T)$ can be obtained starting from $R_{AA}^{incl}(p_T)$ as:

$$\begin{aligned}
 \frac{Y_{AA}^{inc}}{T_{AA}\sigma_{pp}^{inc}} &= R_{AA}^{inc} \\
 Y_{AA}^{pro} + Y_{AA}^{npro} &= R_{AA}^{inc} T_{AA} (\sigma_{pp}^{pro} + \sigma_{pp}^{npro}) \\
 Y_{AA}^{pro} &= R_{AA}^{inc} T_{AA} \sigma_{pp}^{pro} + R_{AA}^{inc} T_{AA} \sigma_{pp}^{npro} - Y_{AA}^{npro} \\
 \frac{Y_{AA}^{pro}}{T_{AA}\sigma_{pp}^{pro}} &= \frac{1}{T_{AA}\sigma_{pp}^{pro}} (R_{AA}^{inc} T_{AA} \sigma_{pp}^{pro} + R_{AA}^{inc} T_{AA} \sigma_{pp}^{npro} - Y_{AA}^{npro}) \\
 R_{AA}^{pro} &= R_{AA}^{inc} + \frac{R_{AA}^{inc} T_{AA} \sigma_{pp}^{npro}}{T_{AA}\sigma_{pp}^{pro}} - \frac{Y_{AA}^{npro}}{T_{AA}\sigma_{pp}^{pro}} \\
 R_{AA}^{pro} &= R_{AA}^{inc} + R_{AA}^{inc} f_B - \frac{Y_{AA}^{npro} \sigma_{pp}^{npro}}{T_{AA}\sigma_{pp}^{pro} \sigma_{pp}^{npro}} \\
 R_{AA}^{pro} &= R_{AA}^{inc} + R_{AA}^{inc} f_B - R_{AA}^{npro} f_B,
 \end{aligned} \tag{B.1}$$

where f_B is the fraction of non-prompt J/ψ to prompt J/ψ measured in pp collisions, and R_{AA}^{npro} is the suppression factor of B-hadron production in Pb-Pb collisions. The fraction of non-prompt J/ψ to prompt J/ψ $F_b = \frac{f_B}{1+f_B}$ is more commonly used. The subscripts *inc*, *pro* and *npro* refer to the inclusive, prompt and non-prompt production of J/ψ.

The differential cross-sections of non-prompt and prompt J/ψ cross-sections as a function of p_T and y have been measured by the LHCb collaboration in pp collisions $\sqrt{s_{NN}} = [7 \text{ TeV}]$ [11] in a kinematic range overlapping with the muon spectrometer. Thus one can extract f_B very precisely from these data as shown on Fig. B.1 where a fit of the p_T and y dependence of this ratio is also given. The integrated

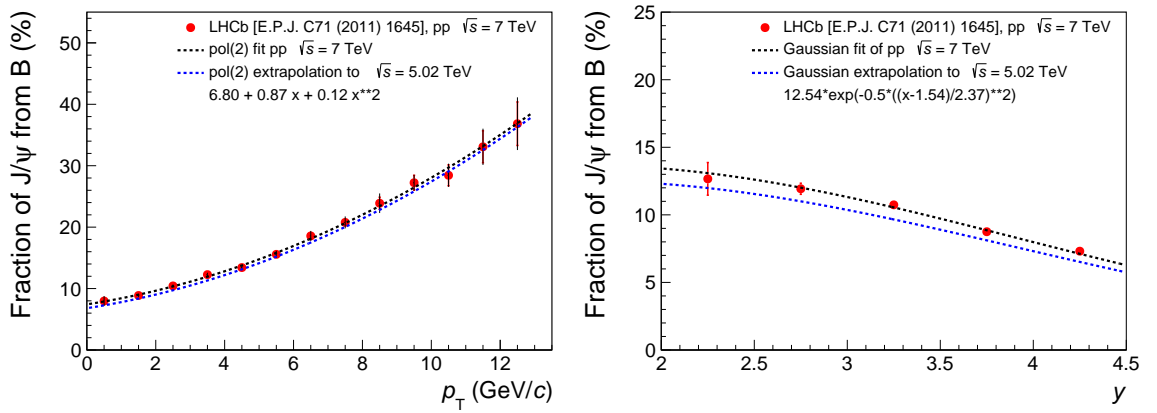


Fig. B.1: Fraction of non-prompt J/ψ to prompt J/ψ, f_B , measured as a function of p_T (left) and rapidity (right). See text for details.

Centrality	R_{AA}^{inc}	F_b	$R_{AA}^{npro} = 1.2$	$R_{AA}^{npro} = 1.0$	$R_{AA}^{npro} = 0.5$	$R_{AA}^{npro} = 0.0$
0-90%	0.69	0.0889	-7.21%	-4.38%	2.69%	9.76%
0-10%	0.66	0.0889	-7.93%	-4.98%	2.39%	9.76%
10-20%	0.67	0.0889	-7.72%	-4.81%	2.48%	9.76%
20-30%	0.69	0.0889	-7.29%	-4.45%	2.66%	9.76%
30-40%	0.66	0.0889	-8.09%	-5.12%	2.32%	9.76%
40-50%	0.74	0.0889	-6.02%	-3.39%	3.18%	9.76%
50-60%	0.79	0.0889	-5.05%	-2.58%	3.59%	9.76%
60-70%	0.92	0.0889	-2.93%	-0.81%	4.47%	9.76%
70-80%	1.12	0.0889	-0.67%	1.07%	5.41%	9.76%
80-90%	1.28	0.0889	0.65%	2.16%	5.96%	9.76%

Table B.1: Values of the difference, in percentage, of the R_{AA}^{npro} with respect to the R_{AA}^{inc} for four values of R_{AA}^{npro} as a function of centrality in Pb–Pb collisions at $\sqrt{s} = 5.02$ TeV. The central values of R_{AA}^{inc} and F_b are also given.

605 measurement, for unpolarized J/ ψ is f_B ($\sqrt{s} = 7$ TeV, $p_T < 14$ GeV/c, $2.0 < y < 4.5$) = $(10.84 \pm 0.04 \pm 1.41)\%$ and f_B ($\sqrt{s} = 7$ TeV, $p_T < 13$ GeV/c, $2.5 < y < 4.0$) = $(10.67 \pm 0.04 \pm 1.41)\%$. More recently, the LHCb collaboration completed the previous measurement with a lower energy at $\sqrt{s} = 2.76$ TeV [12]. The quoted value for unpolarized J/ ψ is f_B ($\sqrt{s} = 2.76$ TeV, $p_T < 12$ GeV/c, $2.0 < y < 4.5$) = $(7.7 \pm 0.7 \pm 0.8)\%$. At $\sqrt{s} = 5.02$ TeV f_B can be calculated from the interpolated cross sections of prompt and
610 non-prompt [13] J/ ψ , resulting in f_B ($\sqrt{s} = 5.02$ TeV, $p_T < 12$ GeV/c, $2.5 < y < 4.0$) = $(9.8 \pm 0.8)\%$. Thus, one can extract a reduction factor in the f_B of 1.41 going from $\sqrt{s} = 7$ TeV to $\sqrt{s} = 2.76$ TeV and of 1.09 from 7 to 5.02 TeV. We will assume in the following that (i) this \sqrt{s} scaling factor is independent of p_T and y for the kinematic range considered (ii) the p_T dependence of f_B can be parametrized with a pol(2) function and (iii) the y dependence of f_B can be parametrized with a Gaussian function. Fig. B.1
615 shows the extrapolation of f_B down to $\sqrt{s} = 5.02$ TeV (blue dashed lines) for the three hypothesis given before. The p_T and y parametrizations of f_B can now be injected in equation B.1.

A reliable determination of the B-quenching factor R_{AA}^{npro} presents more difficulties. At high- p_T for $y < 2.4$, the CMS collaboration has measured the non-prompt J/ ψ suppression [14] in Pb-Pb collisions. For J/ ψ $\langle p_T \rangle \approx 9$ GeV/c, a $R_{AA} = 0.37 \pm 0.08$ (stat.) ± 0.02 (syst.) has been measured.
620 From simulation, one can determine that a 10 GeV/c J/ ψ corresponds to a B-hadron of about 13 GeV/c. Preliminary results with 2011 data analysis (<http://cdsweb.cern.ch/record/1472735/files/HIN-12-014-pas.pdf>, figure 7) show a clear trend of the non-prompt J/ ψ R_{AA} to increase when the p_T decreases. Numerically J/ ψ $R_{AA} \approx 0.3$ (0.5) for a J/ ψ p_T equal to 17 (7) GeV/c. However, we need to assess the B-quenching factor in the p_T and y range where we measure the J/ ψ and no such
625 results are available.

Another input is coming from theoretical prediction coupled with the ALICE measurement of D meson R_{AA} . Radiative energy loss theoretical predictions suggest different suppression factor for heavy quarks according to $R_{AA}^B > R_{AA}^D$. The ALICE measurement [15] shows that D mesons can be suppressed down to $R_{AA} \sim 0.2$ in most central Pb-Pb collisions.

630 In the following tables we have tested four values of R_{AA}^{npro} , 0.0, 0.5, 1.0, and 1.2, keeping the chosen value constant as a function of p_T and centrality. To estimate the effect on $r = R_{AA}(5.02 \text{ TeV})/R_{AA}(2.76 \text{ TeV})$ we adopt the same of R_{AA}^{npro} for both energies.

As a function of centrality, assuming for $R_{AA}^{npro} = 1$ (no quenching of B-hadrons), the direct J/ ψ R_{AA} could be 5% lower than the inclusive J/ ψ R_{AA} for the 0%–10% most central collisions. This difference
635 vanishes when going towards more peripheral collisions. If the B-hadrons quenching is maximum ($R_{AA}^{npro} = 0.0$), the inclusive J/ ψ R_{AA} would be 10% higher.

$p_T(\text{GeV}/c)$	R_{AA}^{inc}	F_b	$R_{AA}^{npro} = 1.2$	$R_{AA}^{npro} = 1.0$	$R_{AA}^{npro} = 0.5$	$R_{AA}^{npro} = 0.0$
0.0-1.0	0.77	0.0677	-4.01%	-2.13%	2.57%	7.27%
1.0-2.0	0.74	0.0773	-5.28%	-3.00%	2.69%	8.38%
2.0-3.0	0.70	0.0886	-7.04%	-4.25%	2.74%	9.72%
3.0-4.0	0.57	0.1016	-12.67%	-8.68%	1.32%	11.32%
4.0-5.0	0.56	0.1162	-14.87%	-10.20%	1.47%	13.14%
5.0-6.0	0.45	0.1321	-25.27%	-18.52%	-1.65%	15.21%
6.0-7.0	0.43	0.1491	-31.84%	-23.61%	-3.04%	17.53%
7.0-8.0	0.38	0.1672	-42.82%	-32.34%	-6.13%	20.08%
8.0-9.0	0.44	0.1861	-39.35%	-28.98%	-3.06%	22.86%
9.0-10.0	0.33	0.2057	-69.72%	-53.78%	-13.94%	25.89%
10.0-12.0	0.41	0.2360	-59.08%	-44.09%	-6.60%	30.89%

Table B.2: Values of the difference, in percentage, of the R_{AA}^{pro} with respect to the R_{AA}^{inc} for four values of R_{AA}^{npro} as a function of transverse momentum in Pb-Pb collisions at $\sqrt{s} = 5.02$ TeV. The central values of R_{AA}^{inc} and F_b are also given.

Centrality	r^{inc}	$F_b(5.02 \text{ TeV})$	$F_b(2.76 \text{ TeV})$	$R_{AA}^{npro} = 1.2$	$R_{AA}^{npro} = 1.0$	$R_{AA}^{npro} = 0.5$	$R_{AA}^{npro} = 0.0$
0-90	1.19	0.0889	0.0713	1.08%	1.24%	1.61%	1.93%
0-10	1.19	0.0889	0.0713	1.02%	1.20%	1.59%	1.93%
10-20	1.17	0.0889	0.0713	0.74%	0.97%	1.48%	1.93%
20-30	1.15	0.0889	0.0713	0.48%	0.75%	1.38%	1.93%
30-40	1.14	0.0889	0.0713	0.22%	0.54%	1.28%	1.93%
40-50	1.22	0.0889	0.0713	1.54%	1.62%	1.78%	1.93%
50-60	1.09	0.0889	0.0713	-0.02%	0.34%	1.18%	1.93%
60-70	1.10	0.0889	0.0713	0.39%	0.67%	1.33%	1.93%
70-80	1.32	0.0889	0.0713	2.59%	2.47%	2.19%	1.93%
80-90	1.17	0.0889	0.0713	1.40%	1.49%	1.72%	1.93%

Table B.3: Values of the difference, in percentage, of the r^{pro} with respect to the r^{inc} for four values of R_{AA}^{npro} as a function of centrality in Pb-Pb collisions at $\sqrt{s} = 5.02$ TeV. The central values of r^{inc} and F_b are also given.

$p_T (\text{GeV}/c)$	r^{inc}	$F_b(5.02 \text{ TeV})$	$F_b(2.76 \text{ TeV})$	$R_{AA}^{npro} = 1.2$	$R_{AA}^{npro} = 1.0$	$R_{AA}^{npro} = 0.5$	$R_{AA}^{npro} = 0.0$
0.0-8.0	1.19	0.0889	0.0713	1.08%	1.24%	1.61%	1.93%
0.0-1.0	1.19	0.0677	0.0543	1.04%	1.11%	1.28%	1.44%
1.0-2.0	1.20	0.0773	0.0642	1.33%	1.34%	1.39%	1.42%
2.0-3.0	1.32	0.0886	0.0758	4.00%	3.49%	2.36%	1.40%
3.0-4.0	1.33	0.1016	0.0892	7.15%	5.89%	3.34%	1.38%
4.0-5.0	1.31	0.1162	0.1041	9.63%	7.68%	3.98%	1.36%
5.0-6.0	1.33	0.1321	0.1205	19.81%	14.44%	6.11%	1.34%
6.0-8.0	1.18	0.1580	0.1471	16.84%	11.36%	4.53%	1.30%

Table B.4: Values of the difference, in percentage, of the r^{pro} with respect to the r^{inc} for four values of R_{AA}^{npro} as a function of transverse momentum in Pb-Pb collisions at $\sqrt{s} = 5.02$ TeV. The central values of r^{inc} and F_b are also given.

Since F_b increase with the J/ψ transverse momentum, B-hadrons decay would have a significant effect at high p_T . Assuming $R_{AA}^{npro} = 1$, the direct J/ψ R_{AA} could be lower than the inclusive J/ψ R_{AA} by 2%, 30%, and 45% at $0 < p_T < 1$ GeV/c, $6 < p_T < 8$ GeV/c, and $10 < p_T < 12$ GeV/c, respectively. Assuming $R_{AA}^{npro} = 0$, the direct J/ψ R_{AA} could be higher than the inclusive J/ψ R_{AA} by 7%, 20%, and 30% at $0 < p_T < 1$ GeV/c, $6 < p_T < 8$ GeV/c, and $10 < p_T < 12$ GeV/c, respectively.

Applying the same assumption on $R_{AA}^{npro} = 1$ ($R_{AA}^{npro} = 0$) to both energies, r^{pro} will be 1–3% (2%) higher than r^{inc} as a function of centrality. As a function of transverse momentum, the difference between r^{pro} and r^{inc} increases from 1% at $0 < p_T < 1$ GeV/c to about 15% at $6 < p_T < 8$ GeV/c if $R_{AA}^{npro} = 1$, and it is at most 2% if $R_{AA}^{npro} = 0$.

References

- [1] Jaroslav Adam et al. Differential studies of inclusive J/ ψ and $\psi(2S)$ production at forward rapidity in Pb-Pb collisions at $\sqrt{s_{NN}} = 2.76$ TeV. 2015.
- [2] K. Aamodt et al. The ALICE experiment at the CERN LHC. *JINST*, 3:S08002, 2008.
- 650 [3] The ALICE Collaboration. Centrality, rapidity and transverse momentum dependence of J/ ψ suppression in Pb-Pb collisions at $\sqrt{s_{NN}} = 2.76$ TeV. *Phys. Lett.*, B714:314–327, 2014.
- [4] <https://indico.cern.ch/event/533776/contributions/2174218/attachments/1276538/1894131/pag-jpsi2mumu-20160520.pdf>.
- 655 [5] Centrality dependence of the charged-particle multiplicity density at midrapidity in Pb-Pb collisions at $\sqrt{s_{NN}} = 5.02$ TeV. Dec 2015.
- [6] A. Andronic, P. Braun-Munzinger, K. Redlich, and J. Stachel. The statistical model in Pb-Pb collisions at the LHC. *Nucl. Phys.*, A904-905:535c–538c, 2013.
- [7] Xingbo Zhao and Ralf Rapp. Medium Modifications and Production of Charmonia at LHC. *Nucl. Phys.*, A859:114–125, 2011.
- 660 [8] Xiaojian Du and Ralf Rapp. Sequential Regeneration of Charmonia in Heavy-Ion Collisions. *Nucl. Phys.*, A943:147–158, 2015.
- [9] Kai Zhou, Nu Xu, Zhe Xu, and Pengfei Zhuang. Medium effects on charmonium production at ultrarelativistic energies available at the CERN Large Hadron Collider. *Phys. Rev.*, C89(5):054911, 2014.
- 665 [10] E. G. Ferreira. Charmonium dissociation and recombination at LHC: Revisiting comovers. *Phys. Lett.*, B731:57–63, 2014.
- [11] R. Aaij et al. Measurement of J/ ψ production in pp collisions at $\sqrt{s} = 7$ TeV. *Eur. Phys. J.*, C71:1645, 2011.
- 670 [12] R Aaij et al. Measurement of J/ ψ production in pp collisions at $\sqrt{s} = 2.76$ TeV. *JHEP*, 02:041, 2013.
- [13] ALICE and LHCb Collaborations. Reference pp cross-sections for J/ ψ studies in proton-lead collisions at $\sqrt{s_{NN}} = 5.02$ TeV and comparisons between ALICE and LHCb results. 2013.
- [14] Serguei Chatrchyan et al. Suppression of non-prompt J/ ψ , prompt J/ ψ , and Y(1S) in PbPb collisions at $\sqrt{s_{NN}} = 2.76$ TeV. *JHEP*, 05:063, 2012.
- 675 [15] Betty Abelev et al. Suppression of high transverse momentum D mesons in central Pb-Pb collisions at $\sqrt{s_{NN}} = 2.76$ TeV. *JHEP*, 09:112, 2012.